Simultaneous targeting of primary tumor, draining lymph node, and distant metastases through high endothelial venule-targeted delivery

Liwei Jiang, Sungwook Jung, Jing Zhao, Vivek Kasinath, Takaharu Ichimura, John Joseph, Paolo Fiorina, Andrew S Liss, Khalid Shah, Nasim Annabi, et al.

▶ **To cite this version:**

Liwei Jiang, Sungwook Jung, Jing Zhao, Vivek Kasinath, Takaharu Ichimura, et al.. Simultaneous targeting of primary tumor, draining lymph node, and distant metastases through high endothelial venule-targeted delivery. Nano Today, 2021, 36, pp.101045. 10.1016/j.nantod.2020.101045 . hal-03445338

HAL Id: hal-03445338
https://hal.univ-lille.fr/hal-03445338

Submitted on 23 Nov 2021

HAL is a multi-disciplinary open access archive for the deposit and dissemination of scientific research documents, whether they are published or not. The documents may come from teaching and research institutions in France or abroad, or from public or private research centers.

L'archive ouverte pluridisciplinaire **HAL**, est destinée au dépôt et à la diffusion de documents scientifiques de niveau recherche, publiés ou non, émanant des établissements d'enseignement et de recherche français ou étrangers, des laboratoires publics ou privés.

Nano Today 36 (2020) 101045

Contents lists available at ScienceDirect

Nano Today

journal homepage: www.elsevier.com/locate/nanotoday

Simultaneous targeting of primary tumor, draining lymph node, and distant metastases through high endothelial venule-targeted delivery

Liwei Jiang[a,1], Sungwook Jung[a,1], Jing Zhao[a], Vivek Kasinath[a], Takaharu Ichimura[b], John Joseph[c], Paolo Fiorina[d], Andrew S. Liss[e], Khalid Shah[f], Nasim Annabi[g,h], Nitin Joshi[c,i], Tomoya O. Akama[j], Jonathan S. Bromberg[k], Motohiro Kobayashi[l], Kenji Uchimura[m,n], Reza Abdi[a,*]

[a] Transplantation Research Center, Renal Division, Brigham and Women's Hospital, Harvard Medical School, Boston, MA 02115, USA
[b] Renal Division, Brigham and Women's Hospital, Harvard Medical School, Boston, MA 02115, USA
[c] Center for Nanomedicine, Department of Anesthesiology, Perioperative and Pain Medicine, Brigham and Women's Hospital, Harvard Medical School, Boston, MA 02115, USA
[d] Division of Nephrology, Boston Children's Hospital, Harvard Medical School, Boston, MA 02115, USA
[e] Department of Surgery and the Andrew L. Warshaw, MD Institute for Pancreatic Cancer Research, Massachusetts General Hospital, Harvard Medical School, Boston, MA 02115, USA
[f] Center for Stem Cell Therapeutics and Imaging, Department of Neurosurgery, Brigham and Women's Hospital, Harvard medical School, Boston, MA 02115, USA
[g] Department of Chemical and Biomolecular Engineering, University of California, Los Angeles, CA 90095, USA
[h] Department of Bioengineering, University of California, Los Angeles, Los Angeles, CA 90095, USA
[i] Koch Institute for Integrative Cancer Research, Massachusetts Institute of Technology, Cambridge, MA 02139, USA
[j] Department of Pharmacology, Kansai Medical University, Osaka 570-8506, Japan
[k] Departments of Surgery and Microbiology and Immunology, University of Maryland School of Medicine, Baltimore, MD 21201, USA
[l] Department of Tumor Pathology, Faculty of Medical Sciences, University of Fukui, Fukui 910-1193, Japan
[m] Department of Biochemistry, Nagoya University Graduate School of Medicine, Nagoya 466-8550, Japan
[n] CNRS, UMR 8576, Unit of Glycobiology Structures and Functions, University of Lille, F-59000 Lille, France

ARTICLE INFO

Article history:
Received 27 June 2020
Received in revised form 8 November 2020
Accepted 26 November 2020
Available online xxxx

Keywords:
Targeting delivery
Caner therapy
HEV antibody

ABSTRACT

Cancer patients with malignant involvement of tumor-draining lymph nodes (TDLNs) and distant metastases have the poorest prognosis. A drug delivery platform that targets the primary tumor, TDLNs, and metastatic niches simultaneously, remains to be developed. Here, we generated a novel monoclonal antibody (MHA112) against peripheral node addressin (PNAd), a family of glycoproteins expressed on high endothelial venules (HEVs), which are present constitutively in the lymph nodes (LNs) and formed ectopically in the tumor stroma. MHA112 was endocytosed by PNAd-expressing cells, where it passed through the lysosomes. MHA112 conjugated antineoplastic drug Paclitaxel (Taxol) (MHA112-Taxol) delivered Taxol effectively to the HEV-containing tumors, TDLNs, and metastatic lesions. MHA112-Taxol treatment significantly reduced primary tumor size as well as metastatic lesions in a number of mouse and human tumor xenografts tested. These data indicate that human metastatic lesions contain HEVs and provide a platform that permits simultaneous targeted delivery of antineoplastic drugs to the three key sites of primary tumor, TDLNs, and metastases.

Published by Elsevier Ltd.

Introduction

The development of antibody-drug conjugates (ADCs) as efficient targeting agents for cancer therapy has created much excitement. Over 100 ADCs are in preclinical development, more than 60 are in clinical development, and three are Food and Drug Administration (FDA)-approved currently for cancer therapy [1–3]. ADCs consist of monoclonal antibodies (mAbs) connected by a specified linkage to

* Correspondence to: Transplantation Research Center, Renal Division, Brigham and Women's Hospital, Harvard Medical School, 221 Longwood Ave, Boston, MA 02115, USA.
E-mail address: rabdi@rics.bwh.harvard.edu (R. Abdi).
[1] LJ and SJ contributed equally to this work.

https://doi.org/10.1016/j.nantod.2020.101045
1748-0132/Published by Elsevier Ltd.

antitumor cytotoxic drugs. ADCs stand in contrast to the traditional methods of cancer therapy (chemotherapy, radiotherapy, antibody immunotherapy, and targeted therapies based on nanoparticles), for which efficacy has been hindered by troubling safety profiles [4]. Indeed, ADCs have been utilized successfully for cancer therapy in recent years [5–8].

High endothelial venule (HEV) is a highly specialized blood vessel found primarily in the lymph nodes (LNs) [9]. Peripheral node addressin (PNAd) is a family of sulfated and fucosylated glycoproteins expressed exclusively on HEVs that is recognized by the monoclonal antibody, MECA79 [9,10]. Interestingly, HEVs also have been incredibly recognized to be formed ectopically within the tumor environment in numerous cancer models [11–14]. However, there is no evidence on generation of HEVs in metastatic lesions.

Remodeling of the stromal compartment of tumor-draining LNs (TDLNs), especially the novel growth of intranodal lymphatic vessels, may accelerate the spread of a tumor to more distant LNs [15,16]. Metastases to LNs is a well-known poor prognostic factor for many solid malignancies [17,18]. Cancer cells migrate from the primary tumor to adjacent LNs through invasion of the surrounding lymph vessels, forming an organized colony in the LNs that becomes a source of dissemination (distant metastasis) to other organs [19]. Importantly, TDLNs are major sites for mounting tumor immunity, where antigen-specific immune responses are directed against tumor cells [20]. TDLNs have been found to contain an immunosuppressive environment when metastases are present [21,22]. TDLNs involvement can, therefore, have an impact on tumor progression in a number of ways.

In addition to the delivery of chemotherapy drugs, targeted delivery of immune checkpoint inhibitors or cancer cell-specific antigens to TDLNs also have the potential to improve cancer therapies [23–25] by eradicating metastatic disease from LNs and increasing tumor immunity, respectively [26]. However, only a small fraction of systemically delivered therapeutics accumulate in the LNs [19,27,28]. Several attempts have been undertaken to enhance the drug delivery pharmacokinetics to the TDLNs through administration of payloads directly to lymphatic vessels (not through the intravenous [i.v.] route) or the LNs themselves [23,29,30]. However, most of these strategies face significant technical limitations.

In addition to TDLNs involvement, distant metastases account for the majority of cancer-associated deaths [31,32]. Typically, strategies such as immunotherapy, radiation therapy, surgery, or a combination thereof [33], fail to halt the progression of metastatic cancers. Furthermore, high-dose systemic chemotherapeutic drugs for metastatic cancer can cause significant toxicity and intolerance for the patients [34,35]. Just a minority of metastasis-specific targets have been exploited therapeutically, so effective prevention as well as suppression of metastatic disease remains an elusive goal [36]. Drugs that reach well-vascularized primary tumors may not accumulate in metastases that are poorly vascularized [26,37,38]. Clearly, a targeted therapy platform using a simple intravenous injection that delivers a drug simultaneously to the primary tumor, TDLNs, and distant metastases would represent a major paradigm-shifting approach to improve the outcomes of lethal cancers.

Here, we isolated and characterized a new anti-PNAd monoclonal antibody called MHA112 by immunizing GlcNAc6ST-1,2,4 triple-knockout mouse, a novel PNAd-deficient model with PNAd-expressing CHO cells. MHA112 demonstrated better affinity than MECA-79, an antibody used widely for PNAd binding. Our MHA112 delivery platform permitted the targeted delivery of cytotoxic agents to the triad of crucial sites for effective antineoplastic therapy—the primary tumor, TDLNs, and distant metastases. Notably, we also demonstrated the potential utility of MHA112 as an imaging agent that can enhance the accuracy of cancer staging by increasing the sensitivity of detecting malignant involvement of the LNs. Treatment with MHA112-Taxol suppressed growth of murine breast cancer model, as well as both murine and human pancreatic cancer. Moreover, LN-targeted delivery via MHA112 restored host immunity to tumors and halted the growth of metastatic lesions as well as fibrosis within the TDLNs.

Results

Generation, characterization and bio-distribution of MHA112

GlcNAc6ST1,2,4 triple-knockout (TKO) mouse, a new PNAd-deficient model, was generated by interbreeding GlcNAc6ST1,2 double deficient mice [39] and GlcNAc6ST4 single deficient mice. To generate novel antibodies targeting HEVs, we immunized GlcNAc6ST-1,2,4 TKO mice three times with 1×10^7 PNAd-expressing CHO (CHO-PNAd) cells [40] (Fig. 1A). After single-clone screening, one clone designated as MHA112 bound successfully to CHO-PNAd cells (Fig. S1A) and HEVs in mouse LNs as well as human tonsil (Fig. 1B). The staining results were similar to commercial anti-HEV antibody MECA-79, which was used as a positive control (Fig. S1A). Isotyping ELISA results indicated that MHA112 mAb was a mouse IgM isotype antibody (Fig. S1B). Then, cell-based ELISA was performed to compare the binding affinity of MHA112 to MECA-79. CHO-PNAd antigen was coated onto 96-well plates and incubated either with MHA112 or MECA79. As shown in Fig. 1C, best-fit curves for the binding affinities of MHA112 and MECA-79 were constructed, and the Kd values were calculated as 0.97 nM and 1.41 nM, respectively. These results indicated that the binding affinity of MHA112 was 30% higher than MECA-79.

One of the key aspects of ADC and drug delivery relies on the internalization of the antibody inside the target cells and transferring to the lysosomes where the linker is cleaved, and the drug of interest is released. Isolating and culturing HEV is a daunting task. We therefore examined whether PNAd expressing CHO cells can internalize the MHA112 antibody. We incubated CHO-PNAd cells with MHA112 that was labeled with pH-sensitive dye pHAb to investigate whether MHA112 can be internalized by target cells. We found that MHA112-pHAb (red) colocalized with the lysosome marker LAMP1 (green), indicating that MHA112 was located in the lysosomes after internalization (Fig. 1D). In the lysosomes, classically the drug is released from ADC following the cleavage of the linker by proteases [41]. To investigate the internalization of MHA112 by the target cells, we performed intracellular staining for flow cytometry at different time points, as described previously [42]. As shown in Fig. 1E, the intracellular levels of MHA112 rose quickly within 4 h of incubation, peaked around 6 h, and slowly decreased through 30 h. Clathrin- and caveolin-dependent pathways are the major routes for the endocytosis of a wide variety of molecules by endothelial cells [43,44]. We investigated the identity of the internalization pathway for MHA112 in CHO-PNAd cells. Intracellular staining for flow cytometry showed that MHA112 was internalized readily by CHO-PNAd cells in the control group (DMSO) (Fig. 1F). The MHA 112 signal was not significantly different from the control group in the presence of caveolae-mediated endocytosis inhibitors [methyl-beta-cyclodextrin (MβC) and nystatin] and a pinocytosis inhibitor (amiloride). In contrast, MHA112 endocytosis was decreased dramatically by the clathrin-mediated endocytosis inhibitor chlorpromazine. These data indicated that MHA112 was internalized through a clathrin-dependent route.

Finally, we tested the LN-targeting capacity and biodistribution of MHA112 in mice by labeling MHA112 with the near-infrared marker IRDye 800CW (MHA112-IR800). First, fluorescence imaging showed that MHA112 conjugation did not impact the fluorescence of the IR800 probe (Fig. S1C). Control mice were injected with an equal amount of free IR800 dye. The mice were euthanized at time points between 6 h and 7 days post-injection. Whole-organ fluorescent

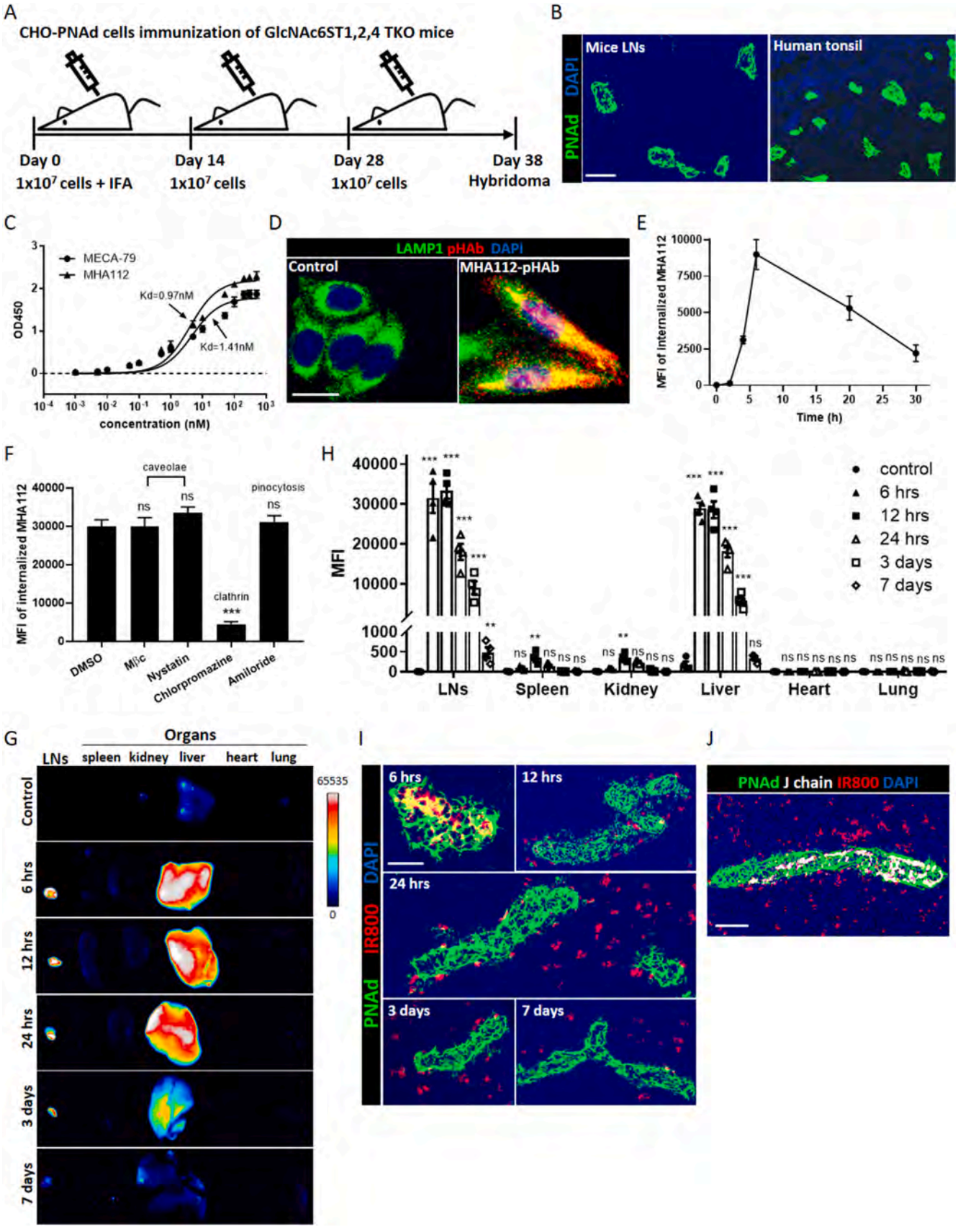

(caption on next page)

Fig. 1. Generation, characterization and bio-distribution of MHA112. (A) Immunization Schedule. GlcNAc6ST1,2,4 TKO mice were immunized three times at intervals of 14 days (primary immunization with 1×10^7 CHO-PNAd cells and IFA, followed by boosting with 1×10^7 CHO-PNAd cells), and spleens were collected for hybridoma generation at 10 days following the third immunization. (B) Fluorescence micrographs showed HEVs (green) in mice LNs and human tonsil were stained by MHA112. DAPI (blue) was cell nuclei. Scale bar: 50 μm. (C) Determination of binding affinity of MECA-79 and MHA112 mAb to CHO-PNAd by cell-based ELISA. Data are representative of three independent experiments (n = 3). (D) Fluorescence micrograph showed colocalization of MHA112-pHAb (red) with lysosome marker LAMP1 (green). DAPI (blue) was cell nuclei. Scale bar: 10 μm. (E) Flow cytometry MFI showed time-dependent changes in intracellular levels of MHA112 in CHO-PNAd cells. Data are representative of three independent experiments (n = 3). (F) Flow cytometry MFIs of intracellular MHA112 were measured in the presence of caveolae-, clathrin- and pinocytosis-pathway inhibitors. Data are expressed as means ± SEM. ***P < 0.001, NS (no significant difference). (G, H) *In vitro* fluorescence imaging and semiquantitative analysis of whole organs showed the bio-distribution of MHA112-IR800 to LNs and organs at different time points. Data are expressed as means ± SEM. **P < 0.01, ***P < 0.001, NS (no significant difference). (I) Fluorescence micrographs showed the distribution of MHA112-IR800 (red) in the vicinity of HEVs (green) in the LNs at different time points. DAPI (blue) was cell nuclei. Scale bar: 20 μm. (J) Fluorescence micrographs showed the distribution of J-chain (MHA112, white) and IR800 (red) in the vicinity of HEVs (green) in the LNs. DAPI (blue) was cell nuclei. Scale bar: 20 μm. (For interpretation of the references to color in this figure legend, the reader is referred to the web version of this article.)

imaging revealed that MHA112-IR800 accumulated mainly in the LNs and liver with very low signals in other organs (Fig. 1G, H). Images of MHA112-IR800 at different time points revealed significant dynamic changes. At 6 h, the signals in the LNs and liver were the highest. Early transient accumulation in the liver was likely due to the nonspecific, innate protein degradative function of this organ. By 3 days, the signal of MHA112-IR800 in the liver faded significantly, while the signal in the LNs persisted. Histological examination of the LNs revealed the presence of MHA112-IR800 (red) inside the HEVs (green) at 6 h (Fig. 1I). From 12 h to 7 days, MHA112-IR800 dispersed from the vicinity of the HEVs (Fig. 1I). We also investigated the identity of the cells that internalized MHA112-IR800. As shown in Fig. S1D, around 40% of the IR800 signal was found in dendritic cells (DCs; $CD11c^+$), while a small portion of IR800 was detected in macrophages ($CD11b^+$) and fibroblastic reticular cells (FRCs; podoplanin $[PDPN]^+$ and $ER\text{-}TR7^+$). To assess whether the IR800 signal in the LNs was from cleaved IR800 dye or intact MHA112-IR800 conjugates, we stained the LNs of MHA112-IR800-injected mice with an antibody to the J-chain, a protein component of the IgM antibody, to indicate the location of intact MHA112. As shown in Fig. 1J, the J-chain signal was detected within the HEV cells, and the IR800 signal in the LN interstitium did not colocalize with the J-chain. All these data together indicated that MHA112-conjugates were cleaved inside HEV cells, and the cleaved conjugates were accessible to LN-resident cells.

Treatment with MHA112-Taxol suppressed breast tumor LN metastases and tumor growth in vivo

To examine the therapeutic potential of MHA112, we employed a xenograft tumor mouse model derived from the mammary cancer cell line 4T1. First, we established that MHA112-IR800 accumulated in TDLNs by fluorescence imaging to demonstrate its capacity to target LNs following systemic delivery in a mouse breast tumor model (Fig. 2A). We conjugated MHA112 mAbs with Taxol, a chemotherapeutic agent that interferes with the growth and spread of cancer cells. To calculate the conjugation ratio of MHA112 and Taxol, we first conjugated Oregon Green 488-labeled Taxol (Taxol*) to MHA112. Based on the molar extinction coefficients (ε) of MHA112 and Taxol* (ε MHA112: 280 nm = 1.2×10^6 cm^{-1} M^{-1}, ε Taxol*: 500 nm = 4.2×10^4 cm^{-1} M^{-1}), we confirmed that the drug-antibody ratio (DAR) was 3.01 ± 0.23 (Fig. 2B). We also performed a high-performance liquid chromatography (HPLC) assay to evaluate the DAR of MHA112-Taxol. The DAR measured by HPLC was 2.811 ± 0.12 (Fig. S2A), which was consistent with Oregon Green 488-labeled Taxol conjugation. 4T1 mouse mammary tumors cells were implanted in the mammary glands of mice. These mice were injected intravenously (i.v.) with MHA112-Taxol or the equivalent amount of free Taxol (0.5 mg/kg) every other day from days 9–31 post-implantation. A control group was injected with the same volume of phosphate buffered saline (PBS). Expansion of both the HEVs and lymphatic vasculature coincide with greater infiltration of the TDLN by the tumor [19]. Lymphatic vessel expansion is also associated with spread of the tumor to adjacent downstream LNs [45]. To examine HEVs and lymphatics expansion and metastatic lesions in the TDLNs, we stained the TDLNs with a tumor marker (pan-cytokeratin) and various vascular. As shown in Fig. 2C, D, the expansion of HEVs and lymphatic vessels in the TDLNs was lower in the MHA112-Taxol group than the free Taxol or control groups. Fewer cells stained positive for pan-cytokeratin in the MHA112-Taxol group, as compared to the other two groups, indicating that the metastatic lesions in the TDLNs were smaller (Fig. 2C, D). Therefore, MHA112-Taxol treatment reduced the metastases of 4T1 mammary tumor cells to TDLNs.

HEVs in some tumor tissues have been reported to be formed ectopically [11–14]. First, immunofluorescence staining revealed the presence of HEVs in 4T1 mammary tumor tissue (Fig. 2E). To further investigate whether MHA112 also accumulated in tumor tissue, mice bearing 4T1 mammary tumors were injected with MHA112-IR800 at day 25 post-implantation. MHA112-IR800 signal was significantly stronger than the free IR800 dye signal in the 4T1 tumor tissue at 24 h following i.v. injection (Fig. 2F). Tumor growth was suppressed significantly in the mice that received MHA112-Taxol in comparison to the mice that received free Taxol as well as those that received the vehicle (Fig. 2G, H) (**P < 0.01, ***P < 0.001). In addition, metastatic lesions in the lung were less extensive in the mice treated with MHA112-Taxol (Fig. 2I). We also stained the tumor sections of the three groups for HEVs. As shown in Fig. S2B, no significant difference of HEV density (%HEV/DAPI) was found among the three groups. Altogether, these data indicated that MHA112-Taxol suppressed the growth of the primary mammary tumor *in vivo*.

Next, we evaluated the role of the enhanced permeability and retention (EPR) effect on potential non-specificity in the targeting of the 4T1 tumor and TDLNs by MHA112 conjugates through the assessment of the trafficking of an isotype control antibody. Tumor-bearing C57BL/6 mice were injected with free IR800, isotype control-IR800 and MHA112-IR800 (n = 4/group). Tumors, TDLNs, and organs were collected for fluorescence imaging at 24 h post-injection. MHA112-IR800 targeted the TDLN and tumor with significantly greater efficacy than the isotype control (Fig. S2C, D). We also compared the half-life ($t_{1/2}$) of free Taxol, isotype control-Taxol, and MHA112-Taxol. Mice were injected with free Taxol*, IgM isotype control-Taxol*, and MHA112-Taxol*, and the sera were collected at different time points from 0 to 72 h. As shown in Fig. S2E, $t_{1/2}$ of isotype-Taxol* and MHA112-Taxol* were 26.72 h and 24.80 h, respectively, while free Taxol* was 1.98 h. These data indicated that IgM conjugation increased the circulation of Taxol, but it did not affect its localization to the TDLN and tumor. Therefore, the trafficking of MHA112 to the TDLNs and tumor did not correlate to the circulation time or a passive EPR effect. These data indicated collectively that the targeting efficacy of MHA112-Taxol is related directly to the interaction between MHA112 antibody and its ligand PNAd.

LN-targeted delivery of Taxol via MHA112 restored host immunity to tumors and improved the fibrosis of TDLNs

Tumor cells have evolved methods to evade the immune response and suppress immune activation [46,47], so we hypothesized

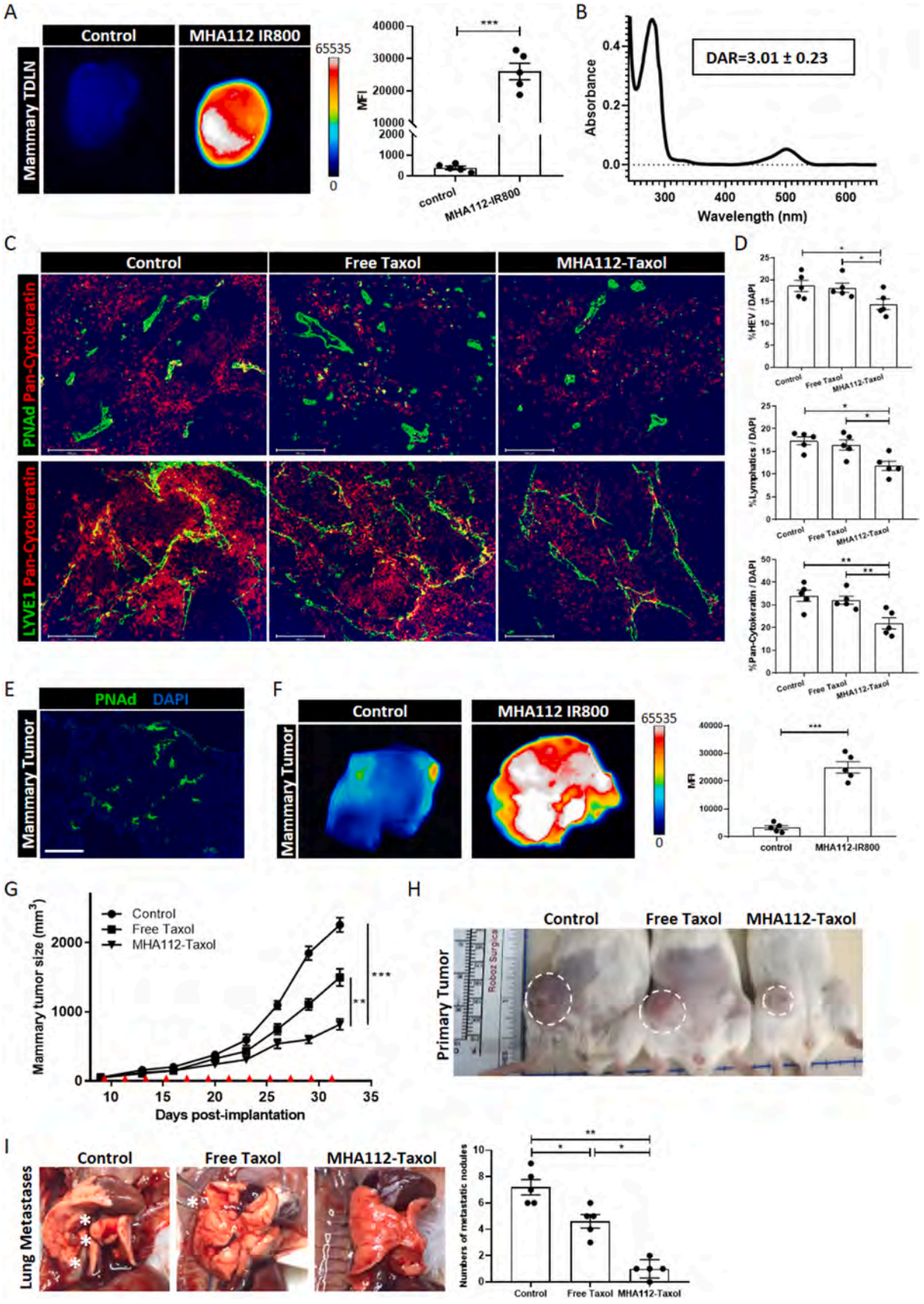

(caption on next page)

Fig. 2. Treatment with MHA112-Taxol suppressed breast tumor LNs metastases and tumor growth *in vivo*. (A) Fluorescence micrographs and semiquantitative analysis showed that MHA112-IR800 mAbs accumulated more robustly in mouse mammary TDLNs at 24 h following i.v. injection in comparison to free IR800. ***P < 0.001. (B) The absorption of MHA112-Taxol* (Oregon Green 488-labeled Taxol) at 280 nm and 500 nm wavelength. Based on the molar extinction coefficients (ε) of MHA112 and Taxol* (ε MHA112: 280 nm = 1.2×10^6 cm^{-1} M^{-1}, ε Taxol*: 500 nm = 4.2×10^4 cm^{-1} M^{-1}), the drug-antibody ratio (DAR) was calculated as 3.01 ± 0.23. (C) Fluorescence micrographs of TDLNs showed less expansion of HEVs (green in upper panel), lymphatic vessels (green in lower panel), as well as fewer metastatic cancer cells (pan-cytokeratin, red) in MHA112-Taxol group than free Taxol and control groups. DAPI (blue) was cell nuclei. Scale bar: 200 μm. (D) Quantification data from two independent experiments with five mice/group (n = 5) are summarized in bar chart. *P < 0.05, **P < 0.01. (E) Fluorescence micrograph revealed the presence of HEVs (green) in 4T1 tumors. DAPI (blue) was cell nuclei. Scale bar: 100 μm. (F) Fluorescence micrographs and semiquantitative analysis indicated that MHA112-IR800 accumulated more robustly in the 4T1 tumors at 24 h following iv injection in comparison to free IR800 dye. ***P < 0.001. (G) Tumor growth curve demonstrated significantly slower growth of 4T1 mouse mammary tumors in the BALB/c-WT mice treated with MHA112-Taxol (n = 12) than free Taxol and control groups (n = 12). Data are expressed as means ± SEM. **P < 0.01, ***P < 0.001. Red triangles indicated the injection timepoints. (H) Representative photographs showed significantly smaller size of 4T1 mouse mammary tumors in the BALB/c-WT mice treated with MHA112-Taxol than free Taxol and control groups. (I) Representative photographs and semiquantitative analysis showed fewer metastatic nodules in the lung in the MHA112-Taxol group. White stars indicated the metastatic lesions. *P < 0.05, **P < 0.01. (For interpretation of the references to color in this figure legend, the reader is referred to the web version of this article.)

that a lower spread of 4T1 to TDLNs combined with more effective delivery of Taxol to TDLNs with MHA112 would be associated with more robust anti-tumor immunity. 4T1 tumor cells were implanted in the mammary glands of mice, and these mice received MHA112-Taxol, free Taxol, or PBS. Flow cytometric analysis of TDLNs revealed higher percentages of $CD8^+CD44^{hi}$ T cells (activated T cells; MHA112-Taxol 72.7% vs free Taxol 49.6% vs control 50.8%) and $CD8^+TNF\alpha^+$ T cells (MHA112-Taxol 56.9% vs free Taxol 40.4% vs control 32.7%), and a lower percentage of $CD4^+CD25^+FoxP3^+$ regulatory T cells (Tregs) (MHA112-Taxol 28.8% vs free Taxol 38.3% vs control 40.8%) in MHA112-Taxol group than free Taxol and control groups (Fig. 3A, B). Moreover, the ratio of $CD8^+TNF\alpha^+$ T cells to Tregs was significantly higher in the MHA112-Taxol group in comparison to the other two groups, indicating a more robust pro-inflammatory immune response (Fig. 3B). We also examined the immune response in the tumors. As shown in Fig. S3, these results were consistent with TDLNs. The percentages of $CD8^+TNF\alpha^+$ and $CD8^+IFN\gamma^+$ T cells were significantly higher, while $CD4^+CD25^+FoxP3^+$ Tregs was lower in the MHA112-Taxol group in comparison to the other two groups.

Fibrosis formed within the tumor, referred to as desmoplastic reaction, is associated with poor prognosis [48,49]. Such phenomenon within the TDLN has received less attention. Examination by fluorescence microscopy of the extracellular matrix (ECM) deposited by stromal cells in the TDLNs revealed that collagen I, fibronectin, and laminin fibers were less extensive in the MHA112-Taxol group (Fig. 3C, D). These data indicated that MHA112-Taxol treatment restored host immunity to the tumors and reduced ECM deposition caused by tumor metastases to the TDLNs.

Next, to assess the efficiency by which MHA112 delivers Taxol to the TLDNs and primary tumors, 4T1 mammary tumor-bearing mice were injected with either MHA112 conjugated to Oregon Green 488-labeled Taxol (Taxol*) or free Taxol* at 25 days post-implantation. At 24 h after injection, more MHA112-Taxol* than free Taxol* accumulated in the TDLNs (Fig. 3E, upper panel). Specifically, more MHA112-Taxol* was located specifically in the vicinity of the HEVs, as compared to free Taxol* group (Fig. 3E, lower panel). In addition, the mean fluorescence intensity (MFI) of Taxol* was significantly higher in the MHA112-Taxol* group, as compared to the free Taxol* group as shown in Fig. 3F (**P < 0.01).

MHA112 imaging identifies early metastasis to the TDLNs

Pursuant to the evidence that MHA112 mAbs localized to the TDLNs, we tested the capacity of MHA112 as a tool to detect metastases to the TDLNs of mammary cancer in mice. 4T1 tumor-bearing mice were injected with MHA112-IR800 at various time points post-implantation, and one group of naive mice was set aside as the control. Fluorescence imaging at 24 h post-implantation revealed no significant difference between MFIs of TDLNs and the control group. However, accumulation of MHA112-IR800 in the TDLNs at 48 h and thereafter until 2 weeks post-implantation became significantly higher than in the control group (***P < 0.001) (Fig. 4A). At 24 h, the expansion of the HEVs in the TDLNs was not significantly different between the two groups (Fig. 4B). However, after 48 h post-implantation, HEVs in the TDLNs expanded significantly over time, especially in comparison to those in the naïve LNs (Fig. 4B) (**P < 0.01, ***P < 0.001). This expansion in HEVs over time was substantiated by significantly higher gene expression of the PNAd core proteins (Glycam1, CD34, Emcn [coding endomucin], Cd300lg [nepmucin], and Podxl [podocalyxin-like protein]) and the modifying enzymes Chst2 (carbohydrate [N-acetylglucosamine 6-O] sulfotransferase 2, GlcNAc6ST1), Chst4 (carbohydrate [N-acetylglucosamine 6-O] sulfotransferase 4, GlcNAc6ST2), and Fut7 (fucosyltransferase 7) in the TDLNs at 2 weeks (Fig. 4C). Moreover, immunofluorescence staining of the TDLNs of other cancers (melanoma, glioblastoma, and lung cancer) revealed that the HEVs were also similarly expanded in these mouse models (Fig. 4D). Together, these data demonstrate that MHA112 can be used to detect early malignant invasion of the TDLNs *in vivo* as well as to evaluate the progress of HEVs expansion in the TDLNs.

Treatment with MHA112-Taxol prolonged survival of mice in a metastatic breast cancer model

A platform for targeted drug delivery to metastatic lesions remains to be developed. To mimic a liver metastases model, 1.0×10^5 4T1 cells were injected directly into the portal vein. First, we confirmed the formation of HEVs in the resulting 4T1 liver masses by immunofluorescence staining (Fig. 5A). These lesions in the liver contained HEVs that arose from blood vasculature, as indicated by positive co-staining with von Willebrand factor (vWF) (Fig. 5A). These data reported the HEVs expression in mouse mammary tumor metastatic lesion.

We also conjugated Taxol to an IgM isotype control to exclude the nonspecific effect of protein degradation of IgM by the liver. Treatments were administered every other day during the first 20 days following injection of the 4T1 cells. The mice that received MHA112-Taxol survived significantly longer (mean survival time [day]; MST = 57) than those that received no treatment, free Taxol, and IgM isotype-Taxol (MST = 33, MST = 37, MST = 36, respectively) (Fig. 5B). Photographs of the livers captured at 20 days following injection indicated that tumors were present in the livers of the untreated, free Taxol, and IgM isotype-Taxol groups, but no macroscopic tumor was observed in the MHA112-Taxol group (Fig. 5C). Another set of identically treated mice was sacrificed 32 days following injection of 4T1 cells, and the tumors in their livers were collected for immunofluorescence staining. As shown in Fig. 5D, immunofluorescence staining of the proliferation marker Ki67 in the 4T1 lesions of the four groups indicated that the proliferation of the cancer cells was lower in the MHA112-Taxol group in comparison to the other groups (Fig. 5D). Moreover,

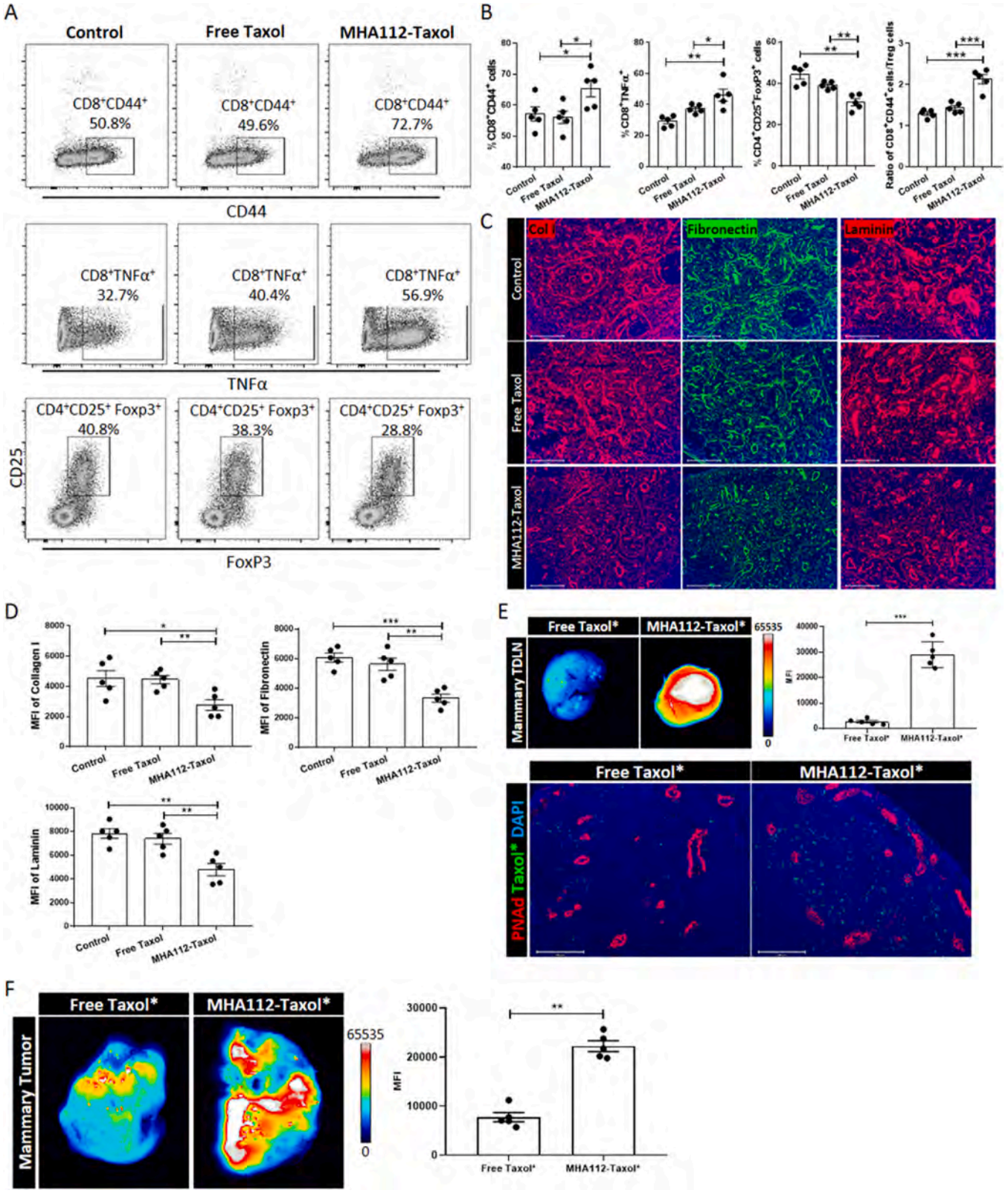

Fig. 3. LN-targeted delivery of Taxol via MHA112 restored host immunity to tumors and improved the fibrosis of TDLNs. (A, B) Representative flow cytometry plots (A) and analysis (B) revealed higher percentages of $CD8^+CD44^+$ T cells and $CD8^+TNF\alpha^+$ T cells, and lower percentage of $CD4^+CD25^+FoxP3^+$ Tregs in TDLNs of MHA112-Taxol than free Taxol and control groups at 25 days post-implantation. All listed populations were gated under $CD3^+CD45^+$ cell population. Data are expressed as means ± SEM. *P < 0.05, **P < 0.01, ***P < 0.001. (C) Fluorescence micrographs of TDLNs revealed that collagen I (red), fibronectin (green), and laminin (red) fibers were significantly sparser in the MHA112-Taxol group than the free Taxol and control groups. Scale bar: 200 μm. (D) Quantification data of collagen I, fibronectin, and laminin from two independent experiments with five mice/group (n = 5) are summarized in bar chart. *P < 0.05, **P < 0.01, ***P < 0.001. (E) Representative *in vitro* fluorescence images and semiquantitative analysis revealed that MHA112-Taxol* accumulated in TDLNs, and fluorescence micrographs of TDLNs revealed higher presence of MHA112-Taxol* (green) within the vicinity of HEVs (red), as compared to the free Taxol* group. Scale bar: 200 μm. ***P < 0.001. (F) The MFI of tumors was significantly higher in MHA112-Taxol* group, as compared to the free Taxol* group (**P < 0.01). The data were presented as mean ± SEM. (For interpretation of the references to color in this figure legend, the reader is referred to the web version of this article.)

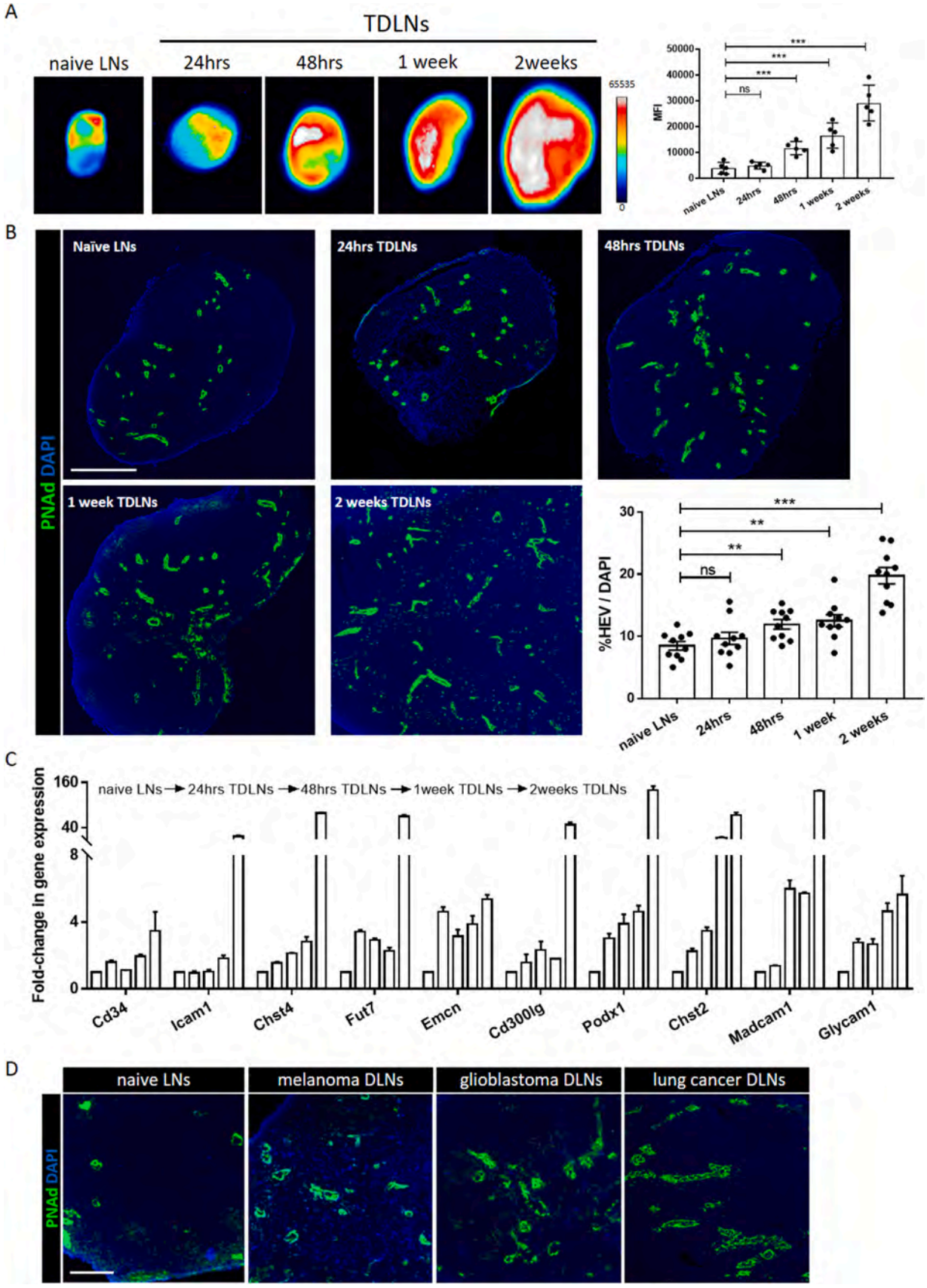

Fig. 4. MHA112 imaging identifies early metastasis to the TDLNs. (A) Fluorescence micrographs and semiquantitative analysis of TDLNs in 4T1 tumor-bearing mice showed accumulation of MHA112-IR800 mAbs 24 h post-injection at 24 h, 48 h, 1 week, and 2 weeks post-tumor implantation in comparison to naïve LNs. ***P < 0.001, NS (no significant difference). (B) Fluorescence micrographs of TDLNs and accompanying semiquantitative analysis display expansion of HEVs (green) at 24 h, 48 h, 1 week, and 2 weeks post tumor implantation, as compared with naïve LNs. Scale bar: 500 μm. Data were presented as mean ± SEM. **P < 0.01, ***P < 0.001, NS (no significant difference). (C) RT-qPCR analysis demonstrated that HEV-related genes were upregulated in TDLNs. (D) Fluorescence micrograph revealed the expansion of HEVs (green) in the TDLNs from melanoma, glioblastoma, and lung cancer-bearing mice. Scale bar: 100 μm. (For interpretation of the references to color in this figure legend, the reader is referred to the web version of this article.)

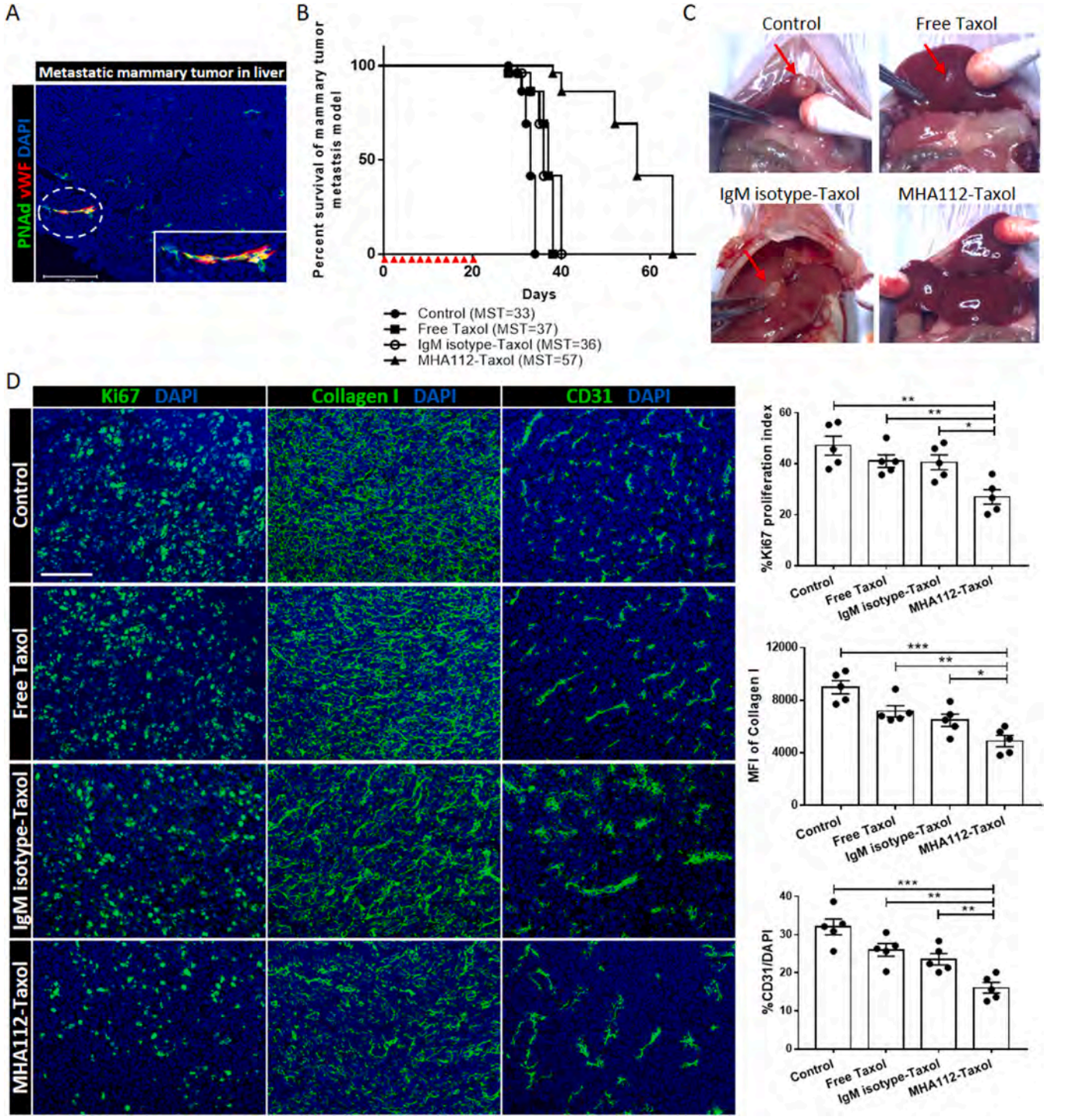

Fig. 5. Treatment with MHA112-Taxol prolonged survival of mice in a metastatic breast cancer model. (A) Fluorescence micrograph of 4T1 tumor in the liver revealed overlapping of vWF$^+$ blood endothelial cells (red) with HEVs (green). Scale bar: 200 μm. (B) Survival curve of metastatic 4T1 breast tumor mouse model showed significantly longer survival of MHA112-Taxol-treated mice (n = 5, MST = 57) than the untreated control, free Taxol and IgM isotype-Taxol-treated groups (n = 5, MST = 33, 37, 36, respectively). Red triangles indicated the injection timepoints. (C) Representative photographs of 4T1 tumors in mouse livers showed significantly smaller size in the MHA112-Taxol group (n = 5) than the other three groups (n = 5). (D) Fluorescence micrographs of metastatic tumor lesions showed lower tumor cell proliferation (Ki67) and ECM accumulation (collagen I), and less expanded vasculature (CD31) in the MHA112-Taxol group than the other groups. Scale bar: 100 μm. Quantification data from two independent experiments with five mice/group (n = 5) are summarized in bar chart. *P < 0.05, **P < 0.01, ***P < 0.001. (For interpretation of the references to color in this figure legend, the reader is referred to the web version of this article.)

deposition of collagen I fibers and expansion of the vasculature were also lower in the MHA112-Taxol group (Fig. 5D). These data indicated that treatment with MHA112-Taxol was effective in reducing the growth of metastatic breast cancer and prolonging survival in these mice.

Treatment with MHA112-Taxol suppressed human and murine pancreatic tumor progression in vivo

Pancreatic cancer has some of the highest mortality rate of all major cancers [50]. After confirming the inhibitory effects of MHA112-Taxol treatment on breast tumors model, we tested its efficacy in suppressing

the growth of human and murine pancreatic tumors in *in vivo* mouse models to increase its robustness in treating lethal tumors and demonstrate its clinical translatability. Panc02 murine pancreatic tumor cells were implanted directly in the pancreas. Treatments were administered every other day during the first 20 days post-implantation. All mice were euthanized at 20 days post-implantation to assess the size of the primary tumor and degree of liver metastases. The pancreatic tumors were significantly smaller in the MHA112-Taxol group than the untreated and free Taxol groups (Fig. 6A, B). We also examined metastatic lesions in the liver, which were smaller in size and significantly reduced in abundance in the MHA112-Taxol group (Fig. 6C, D). Immunofluorescence staining of the primary tumor in the pancreas confirmed the presence of HEVs, which co-stained with the blood vasculature marker vWF (Fig. 6E).

Next, another set of three similarly treated groups of mice were designated for assessment of survival. As shown in Fig. 6F, mice that received MHA112-Taxol survived longer (MST = 45) than those that were received PBS (control) or free Taxol (MST = 32 and MST = 34, respectively). Then, Panc02 cells were implanted subcutaneously to assess directly the effect of MHA112-Taxol on the progression of pancreatic tumor growth. First, we assessed the MHA112 accumulation in mouse pancreatic tumors by fluorescence imaging in Fig. 6G. Mice received the designated treatments every other day from 15 to 44 days following tumor implantation, and the tumors grew more slowly in the mice treated with MHA112-Taxol than those treated with free Taxol or PBS (Fig. 6H).

Finally, we conducted a similar experiment in a patient-derived xenograft tumor of a surgically resected pancreatic ductal adenocarcinoma (PDAC). PDAC tumors were implanted into humanized NOD scid gamma (NSG) mice, which lack LNs. The mice were randomized on the basis of tumor size. Similar to mouse pancreatic tumor, MHA112 also highly accumulated in human PDAC tumor in Fig. 6I. Fig. 6J showed that the PDAC tumors grew more slowly in the mice treated with MHA112-Taxol (equivalent to 0.5 mg/kg of free Taxol) than those treated with free Taxol or PBS. Together, these findings demonstrated that treatment of human and mice pancreatic cancer with MHA112-Taxol was significantly more effective than treatment with free Taxol.

HEV expansion of human TDLNs and presence in human primary tumors and metastatic lesions

To further investigate the use of MHA112 for human cancer therapy, we performed immunohistochemical staining on human TDLNs and human tumor tissues (pancreatic cancer, ovarian cancer, prostate cancer, and gastric cancer). We found that HEV expanded in all human TDLNs tested (Fig. 7A) and that human primary tumor tissues also contained HEVs (Fig. 7B). Consistent with mouse mammary tumor, human primary breast tumor and lung metastatic lesion also had HEV expression (Fig. 7C). In our previous study, we had shown that the PDAC primary tumor contains HEVs [51]. Here, PDAC cells were injected directly into the portal vein of NSG mice (Fig. 7D) to examine if the metastatic lesion of PDAC also has HEVs. In Fig. 7E, The PDAC lesion in the liver showed HEVs structures. Moreover, MHA112-IR800 localized to the vicinity of the HEVs in the PDAC metastatic tumor (Fig. 7E). In Fig. 7F, pancreatic metastatic tumor in human duodenum also showed HEVs. These data indicated that the expansion of HEVs in human TDLNs and the presence of HEVs in various human tumors underlies the potential of MHA112 for translation as both a diagnostic and therapeutic agent to human studies.

Discussion

In this study, we generated a new antibody called MHA112 that targets PNAd expressed by HEV. MHA112 was isolated from a novel PNAd-deficient mouse model that had been immunized with PNAd-expressing CHO cells. MHA112 mAbs showed 30% higher binding affinity compared to MECA-79 and cross activity with human HEVs. The effect of ADCs relies on the internalization of targeting antibody into endosomes that subsequently mature and fuse with lysosomes [52,53]. In the lysosomes, the drug is released via cleavage of the linker by specific proteases or by the degradation of the ADCs. Free drug released from ADCs can cross the plasma membrane to access the extracellular milieu and kill neighbor cells by a process called the bystander effect [54–56]. While isolating HEV endothelia cells and culture are extremely difficult, using PNAd-expressing CHO, we showed that, MHA112 was internalized by target cells and localized in lysosomes *in vitro*. *In vivo* study, we showed that MHA112 has strong LN-targeting activity through HEVs binding. The cleaved conjugates from MHA112 can pass through HEVs endothelial cells into LNs interstitium evidenced by LN residence DCs and FRCs uptake. Clathrin- and caveolin-dependent pathways are the major routes by which endothelial cells internalize a wide variety of molecules [43,44]. Our data showed that MHA112 was internalized via clathrin-dependent endocytosis in the target cells.

Metastasis to the TDLN is a critical prognostic parameter for patients with solid tumors [19]. Indeed, patients with cancer spreading to the LNs have a worse prognosis than those without nodal disease [19,57]. These metastatic foci in the LNs are extremely difficult to treat, as a small fraction of systemically delivered drugs accumulates in LNs [27], even with high-dose systemic chemotherapeutic drugs, which can also cause significant toxicity and intolerance for patients [34,35]. Here, we sought to understand whether MHA112-assisted delivery would improve the trafficking of Taxol to TDLNs. Our data showed that Taxol accumulated more robustly in the TDLNs following conjugation to MHA112, as compared with administration of free Taxol. Concentrating Taxol within the LNs can target rapidly growing metastatic cancer cells and kill them directly. Spread of cancer cells from TDLNs is an important mechanism for the formation of distant metastasis and tumor immunity [19,58,59]. In addition, an increase in fibrosis within the tumor microenvironment has been shown to occur via activation of cancer-associated fibroblasts (CAFs), promoting tumor progression [60,61]. The impact of fibrosis in TDLNs is not as clear. TDLN fibrosis could contribute to poor chemotherapy drug penetration [62–64]. Interestingly, we noted a significant amount of fibrosis in the LNs, contributing potentially lesser to poor penetration of systemically administered Taxol in our experiments. Notably, this fibrosis was significantly less extensive in the mice that were treated with MHA112-Taxol. A nanoparticle formulation of albumin-bound Taxol (Abraxane, or nab-paclitaxel) was found previously to interfere with the function of CAFs in a rat model of intrahepatic cholangiocarcinoma [65] as well as in human pancreatic cancer patients [66], and it also was observed to disrupt the migration of CAFs *in vitro* [67]. A modified nanoparticle formulation of Taxol also inhibited the proliferation of CAFs in a murine pancreatic cancer model [68]. Some cleaved drugs from MHA112 were internalized by FRCs in TDLNs in our study, and we have demonstrated the importance of FRCs to LN fibrosis in previous studies [69–71]. However, whether inhibition by Taxol of ECM secretion by FRCs leads to the reduced fibrosis we observed in the TDLNs of mice treated with MHA112-Taxol is an important question that requires further investigation. Previous studies have examined the link between the formation of tertiary lymphoid organs (TLOs) and cancer outcomes [72]. We are interested in conducting future studies to quantify TLOs as well as HEVs, and examining their association with the progression of slow-growing tumors in mice.

LNs are extremely compartmentalized organs where naïve T cells home via HEVs to interact with potential antigens presented by LN-resident DCs [70,73]. Mounting tumor immunity within TDLNs can not only suppress the tumor burden within the TDLNs, but also reduce spreading to distant peripheral organs [16,74–76]. In this study,

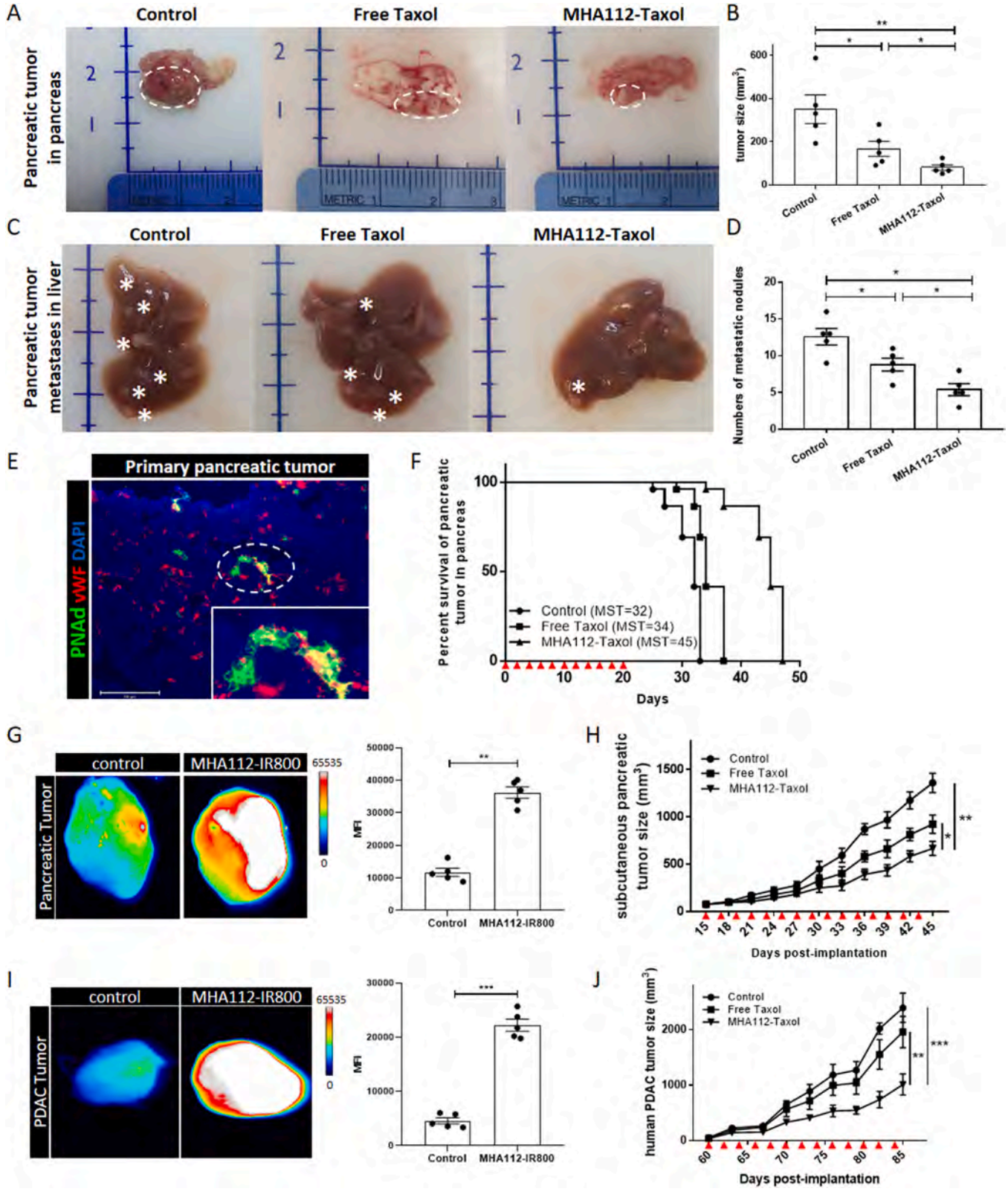

(caption on next page)

Fig. 6. Treatment with MHA112-Taxol suppressed human and murine pancreatic tumor progression *in vivo*. (A, B) Representative photographs (A) and analysis (B) of panc02 pancreatic cancer tumor size in mice revealed significantly smaller size in mice treated with MHA112-Taxol (n = 5) than control and free Taxol groups (n = 5). Data were presented as mean ± SEM. *P < 0.05, **P < 0.01. (C, D) Representative photographs (C) and analysis (D) of metastatic lesions of panc02 in liver showed significantly fewer metastatic nodules in MHA112-Taxol groups. Stars indicated metastatic lesions. Data were presented as mean ± SEM. *P < 0.05. (E) Fluorescence micrograph of primary panc02 tumor in mice revealed the presence of HEVs (green) that co-stain with blood endothelial marker vWF (red). Scale bar: 200 μm. (F) Survival curve of mice implanted with panc02 tumors in the pancreas showed significantly longer survival of those treated with MHA112-Taxol (n = 5, MST = 45) in comparison to control and free Taxol (n = 5, MST = 32, MST = 34, respectively). Red triangles indicated injection timepoints. (G) Fluorescence micrographs and semiquantitative analysis showed that MHA112-IR800 accumulated more robustly in the pancreatic tumor 24 h following iv injection, as compared with free IR800 dye. **P < 0.01. (H) Tumor growth curve demonstrated slower growth of Panc02 mouse pancreas tumors implanted subcutaneously in the C57BL/6-WT mice treated with MHA112-Taxol (n = 10) than control and free Taxol groups (n = 10). Data were presented as mean ± SEM. *P < 0.05, **P < 0.01. Red triangles indicated the injection timepoints. (I) Fluorescence micrographs and semiquantitative analysis showed that MHA112-IR800 accumulated more robustly in PDAC tumor 24 h following i.v. injection, as compared with free IR800 dye. ***P < 0.001. (J) Tumor growth curve showed that the size of PDAC human pancreatic tumors injected subcutaneously in NSG mice treated with free Taxol and MHA112-Taxol (n = 6) were significantly smaller than the control group treated with PBS (n = 6). Data were presented as mean ± SEM. **P < 0.01, ***P < 0.001. Red triangles indicated the injection timepoints. (For interpretation of the references to color in this figure legend, the reader is referred to the web version of this article.)

we found that localization of Taxol inside the LNs was associated with augmentation of the cytotoxic immune response, as demonstrated by increases in the populations of activated and TNFα-secreting $CD8^+$ T cells and inhibition of the anti-inflammatory immune response, as evidenced by a decrease in the population of Tregs. Prior studies have shown that chemokines secreted by the tumor cells within the TDLNs promote recruitment of Tregs, creating a vicious cycle of immunosuppression [73,77–80] and constituting one mechanism by which a high density of Tregs is correlated with poor prognosis for many cancers [81–83]. Increasing the destruction of the cancer cells within the TDLNs via MHA112-assisted drug delivery may permit recovery of their stromal compartments and the mounting of an effective anticancer immune response. The activity of DCs has been identified as fundamental to the effectiveness of the anticancer immune response [84,85] as well as immune checkpoint inhibitor therapy [86]. The previous studies have demonstrated that *in vitro* treatment of DCs with Taxol boosts their capacity for $CD8^+$ T cell proliferation [87], an effect similar to the results we observed in our *in vivo* model. Other studies showed that Taxol promoted the differentiation of myeloid-derived suppressor cells to DCs [88] and upregulated the expression of MHC class II by DCs [89]. Maier et al. showed recently that DCs that internalize tumor-associated antigens adopt an immunosuppressive phenotype marked by expression of programmed death-ligand 1, but this phenotype can be reversed by blockade of IL-4 signaling [90]. The accumulation of cleaved drugs from MHA112 within DC population could increase their allergenicity mounting a stronger anti-tumor immunity.

Altogether, our study highlights the importance of delivering therapeutics to LNs. LNs/lymphatic delivery approach has been the subject of several past studies, but many challenges have hindered its success. A vast majority of the current methods for targeting LNs rely on injection of the payloads into the surrounding skin and passive transport through the lymphatics [91]. Numerous factors, including the size of the injected particles or drugs, determine whether they extravasate via capillaries or lymphatics [91,92]. Some have attempted to target mediastinal lymph nodes by injecting the payloads into the peritoneum of animals and relying on passage through the abdominal lymphatics [93]. Others have injected payloads directly into the LNs [94,95]. Some of these routes pursued, such as direct injection or lymphatic access, may not be practical for widespread use. Furthermore, alterations of interstitial fluid pressure and lymph angiogenesis at the tumor site may interfere with the delivery of the payload. In addition, the TDLNs of many visceral or thoracic tumors are not accessible through injection into the skin. These factors underline the utility of payload delivery to the TDLNs via systemic injection. Our delivery route provides access to all LNs, since all contain HEVs. However, the TDLNs will receive a higher amount of the payload, as they contain HEVs that are more expanded. Therefore, our platform has the remarkable capacity to amplify the accumulation of the payload in TDLNs indiscriminately, downstream LNs, and other LNs throughout the body that have been infiltrated by the cancer and contain expanded HEVs. Whereas we used antibody-coated nanoparticles previously as vehicles for the therapeutic agents in this HEV-targeting platform [96], here we conjugated the therapeutic agent directly to the antibody, thereby increasing its translatability to clinic. Indeed, MHA112 permits the conjugation of a wide range of drugs other than chemotherapeutic agents, including the delivery of immune checkpoint inhibitors or antifibrotic agents, thereby boosting their anticancer efficacy. Attempts have also been made to increase HEV formation [97,98]. Therefore, combining a strategy to increase HEVs with the delivery of chemotherapeutic drugs may form a synergistic route for future cancer therapy.

The formation of HEVs at the primary tumor site has been noted in previous studies. HEVs can be formed in the stromal compartment of solid tumors, including melanomas, breast cancer, ovarian cancer, lung cancer, and PDAC [11–14]. Here, we report that HEVs are formed in primary murine breast tumors. Importantly, we also confirmed the presence of HEVs in various human cancers, such as PDAC and its metastatic lesions, as well as human pancreatic cancer, ovarian cancer, prostate cancer, and gastric cancer. To add more rigor and translation, the human PDAC model was utilized in NSG mice to confirm direct tumor targeting by MHA112, due to a deficiency of LNs in these mice. Tumor growth was suppressed markedly by treatment of these mice with MHA112-Taxol. The survival curve following treatment of these mice showed that MHA112-Taxol prolonged survival significantly in comparison to treatment with free Taxol or IgM isotype-Taxol. In addition, tumor proliferation, tumor-associated ECM deposition, and expansion of the vasculature were also inhibited significantly by treatment with MHA112-Taxol. Notably, PNAd molecules are conserved amongst all mammals, which also emphasizes the clinical translatability of our MHA112-based delivery platform.

In addition to invasion of TDLNs by cancer, distant metastasis constitutes a major challenge to the efficacy of cancer treatment. Distant metastasis is responsible for more than 90% of cancer associated death, as these lesions are extremely difficult to treat [31,99,100]. Typically, effective treatment of metastatic cancer requires systemic therapy to reach cancer cells throughout the body. Increasing the dosage of drugs in order to achieve therapeutic concentrations within metastatic masses results in toxicity and is not tolerated often by patients [24]. Therefore, increasing drug penetration and accumulation specifically at metastatic sites is a new strategy to minimize systemic toxicity [101]. Here, we have reported the formation of HEVs in metastatic lesions in both mouse and preclinical human cancer models. Future studies are required to understand the mechanism by which HEVs form in metastatic masses, perhaps from the proliferation of circulating progenitor cells or the effect of molecules secreted by cancer cells that transform the stromal compartment of the surrounding tissue to support the creation of HEVs. Interestingly, our data showed that treatment with MHA112-Taxol was effective in reducing the growth of metastatic lesions comprised of both breast and pancreatic cancer.

Furthermore, MHA112 permits the detection of the primary tumor, TDLNs, and distant metastases. Detection of the cancer cells in the TDLNs as well as distant metastases is extremely important to

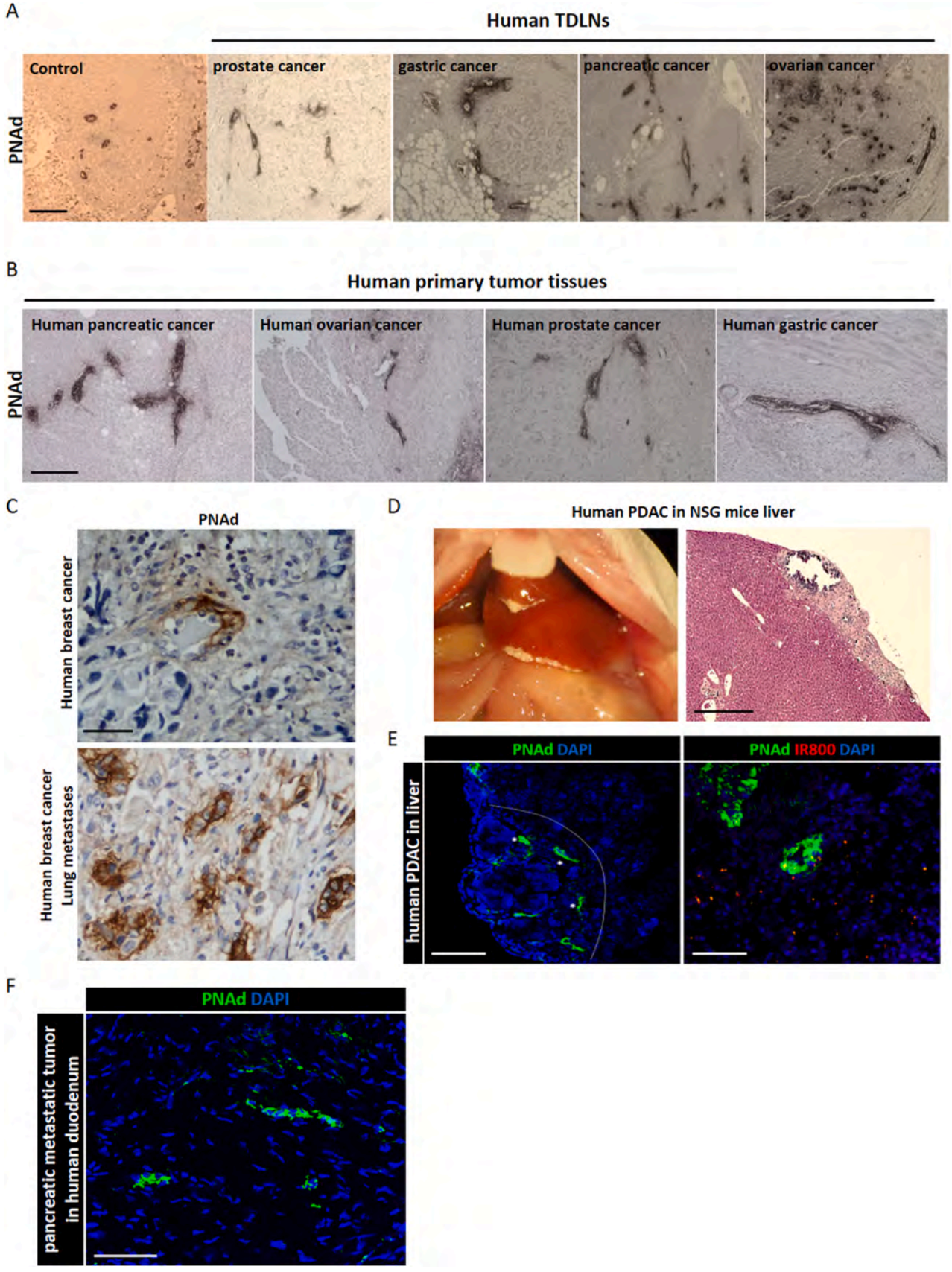

Fig. 7. HEV expansion of human TDLNs and presence in human primary tumors and metastatic lesions. (A) Light micrographs of immunohistochemical staining of TDLNs of various human cancers revealed the expansion of HEVs in pancreatic cancer, ovarian cancer, prostate cancer, and gastric cancer. Scale bar: 200 μm. (B) Light micrographs of immunohistochemical staining of primary tumors of various human cancers revealed the presence of HEVs in pancreatic cancer, ovarian cancer, prostate cancer, and gastric cancer. Scale bar: 200 μm. (C) Light micrographs of immunohistochemical staining of human primary breast cancer and lung metastases lesion revealed the presence of HEVs. Scale bar: 50 μm. (D) Representative photograph and light micrograph of H&E staining of PDAC tumor in liver of NSG mouse. Scale bar: 500 μm. (E) Fluorescence micrographs of metastatic PDAC lesions in liver reveal MHA112-IR800 trafficking (red, scale bar: 100 μm) to HEVs (green, scale bar: 200 μm). (E) Fluorescence micrograph of human pancreatic metastatic lesion in the duodenum revealed the presence of HEVs (green). Scale bar: 100 μm. (For interpretation of the references to color in this figure legend, the reader is referred to the web version of this article.)

accurate staging [102,103]. Since healthy peripheral organs do not have HEVs, the identification of metastatic masses in peripheral tissues by MHA112 conjugated to a tracer, due to the *de novo* presence of HEVs can alter the treatment course dramatically for these patients from the time points of proper staging to metastasis removal. Due to the presence of HEVs in nascent primary tumor and metastatic sites, our HEV-targeting strategy could also strengthen the sensitivity of early tumor detection. Thus, conjugation of a radiographic marker to MHA112 would afford a significant opportunity for future molecular imaging.

Most ADCs are designed directly against specific antigens on tumor cells, so they are limited to select groups of antigen-positive patients. Antigen loss or antigen-low escape may constitute large obstacles to treatment success in solid malignancies, which display high heterogeneity in target antigen expression [104,105]. MHA112 permits superior delivery of Taxol to the key sites of the primary tumor, TDLNs, and metastatic lesions. Poor delivery kinetics of chemotherapy drugs to TDLNs, tumor, and metastatic deposits has constituted a key obstacle to effective direct killing of tumor cells by chemotherapy drugs [27,28]. Taxol kills tumor cells through induction of apoptosis [106]. Accordingly, our data indicate that cancer cells experience a much higher rate of death. Furthermore, our mechanistic data indicate that the anti-tumor immune response in the TDLN was enhanced. Notably, the LN stroma exhibited a less fibrogenic or desmoplastic phenotype as well. This normalization of the LN stroma should support the mounting antitumor immune response. Overall, our innovative HEV-targeted platform provides a novel approach for simultaneous delivery of a payload to three different important sites—primary tumor, metastatic LNs, and metastatic lesions in distant organs—for effective cancer therapy, which constitutes a major urgent clinical need.

Materials and methods

Mice

All animal experiments and methods were performed in accordance with the relevant guidelines and regulations approved by the Institutional Animal Care and Use Committee of Brigham and Women's Hospital in Boston, MA (protocol number: 2016N000167/04977). C57BL/6J (WT) (#000664), BALB/c (WT) (#000651) mice, and NOD.Cg-PrkdcscidIL2rgtm1Wjl/SzJ (NSG) (#005557) mice were purchased from Jackson Laboratory (Bar Harbor, ME, USA) and used at 8–10 weeks of age. GlcNAc6ST1,2,4 TKO mice were generated by crossbreeding GlcNAc6ST1,2,4 triple heterozygous mice that were produced by interbreeding GlcNAc6ST1/GlcNAc6ST2 doubly deficient mice [39] and GlcNAc6ST4 single deficient mice [107].

Cell lines and cell culture

CHO-PNAd cells were generated as described previously [40]. 4T1 mouse breast cancer cells were purchased from American Type Culture Collection (VA, USA). Panc02 mouse pancreatic cancer cells were provided by Dr. Claudia Gravekamp, Albert Einstein College of Medicine (New York, NY). CHO-PNAd cells were cultured in α-MEM with 10% FBS and 1% penicillin/streptomycin (pen/strep). 4T1 cells were cultured in RPMI-1640 medium with 10% FBS and 1% pen/strep. Panc02 cells were cultured in McCoy's medium with 10% FBS, glutamine (2 mM), non-essential amino acids, sodium pyruvate (1 mM), HEPES (10 mM), and pen/strep (100 U/ml). Cells were maintained in a 37 °C incubator at 5% CO_2.

Immunization and hybridoma generation

GlcNAc6ST-1,2,4 TKO mice were immunized with CHO-PNAd cells every other week for 6 weeks. In brief, cell pellet preparation containing 107 cells was emulsified in Incomplete Freund's Adjuvant (IFA) and administered by intraperitoneal (IP) injection. Mice were bled after each boost, and ELISA was used to monitor anti-HEV antibody titers in the serum. The spleens were collected, and cells were released by gentle pressure applied to the capsule of the organ, which was placed between two frosty glass slides. Splenocytes and Myeloma SP2/0 cell line were mixed in a 1:1 ratio, and the hybridoma were generated by electrical cell fusion. The cells were suspended in 15% FBS-RPMI medium (containing 10% BM-Condimed, PS, 2ME, 1x HAT) at the concentration of 1–2 × 105 total cells/ml and seeded in 96-well plates. ELISA against CHO-PNAd was performed. Hybridoma medium alone and secondary antibody served as the negative controls. Immune polyclonal serum and anti-HEV antibody served as the positive controls. Antibodies were plated directly from culture supernatants. Cells from the positive wells were subcloned by limiting dilution to obtain monoclonal lines.

ELISA

CHO-PNAd (2 × 104) cells were coated onto 96-well plates and incubated overnight at 37 °C. After five washes with PBS buffer, the plates were fixed with 4% paraformaldehyde and blocked with 3% BSA. The antibody dilutions starting at 1 ng/ml to 300 μg/ml were then added to the wells. After five washes in PBST, secondary antibodies, HRP–conjugated goat anti-mouse (31430, Invitrogen) and anti-rat (31470, Invitrogen) were added at a 1:10,000 dilution and incubated for 1 h at room temperature. Binding was detected with the addition of TMB substrate (N301, Thermo Scientific), and the reaction was stopped by adding TMB Stop Solution (N600, Thermo Scientific). Absorbance signals were read at 450 nm. Isotyping ELISA was performed using Rapid ELISA Mouse mAb Isotyping Kit (37503, Thermo Scientific).

Antibody internalization assay

MHA112 antibody was labeled with pHAb Reactive Dyes (G9841, Promega) and incubated with CHO-PNAd cells for 2 h at 37 °C. After five washes with PBS buffer, CHO-PNAd cells were stained with Lysosomal Staining Kit (ab112137, Abcam). CHO-PNAd cells were fixed with 4% paraformaldehyde, and DAPI (VECTASHIELD, Vector Laboratories) was used to counterstain the cell nuclei. The cells were visualized using an EVOS™ FL Auto 2 Imaging System (Thermo Fisher Scientific).

Immunofluorescence staining

8-μm tissue sections were cut by cryo-sectioning and stained with conjugated or purified antibodies. Purified antibodies were detected using secondary antibodies. The antibodies included MECA-79 (sc-19602, SCBT), anti-CD11c (117301, BioLegend), anti-CD11b (101202, BioLegend), anti-LYVE1 (ab14917, Abcam), anti-αSMA (19245S, CST), anti-CD31 (14-0311-82, Invitrogen), anti-Collagen I (ab34710, Abcam), anti-Collagen IV (NBP1-91258, Novus), anti-Laminin (ab11575, Abcam), anti-pan-cytokeratin (AE1/AE3, sc-81714, SCBT). DAPI (VECTASHIELD, Vector Laboratories) was used to counterstain the cell nuclei. The stained tissue sections were visualized using an EVOS™ FL Auto 2 Imaging System (Thermo Fisher Scientific). Quantification was performed on 2–3 sections from at least 3 separate mice using image analysis software Celleste (Invitrogen) and ImageJ (NCBI, 1.8.0_112).

In vivo biodistribution studies of antibody

MHA112 antibody was labeled with IRDye 800CW Protein Labeling Kits (928-38040, LI-COR). C57BL/6 mice were used for biodistribution studies. 100 μg of MHA112-IR800 was administered

iv via retro-orbital injection. Trafficking of fluorescent MHA112-IR800 was detected using a UVP iBox Explorer Imaging Microscope, equipped with a 750-to-780-nm excitation filter and an 800-nm long-pass emission filter. LNs and organs were collected and analyzed for the evaluation of the biodistribution of MHA112.

Tumor implantation

Mice were anesthetized with isoflurane, and tumor cell lines (4T1and Panc02) were gently injected subcutaneously in the mammary glands or flanks of mice. 1×10^5 cells were injected per mouse for the 4T1 tumor model. 2×10^6 cells were injected per mouse for the Panc02 tumor model. 1×10^4 4T1 cells were used for portal vein injection. 2×10^6 Panc02 cells were used for pancreas implantation. Human PDAC tumors for research purposes were collected at the University of Massachusetts Medical School under informed consent. The specimens were completely anonymous, had no direct identifiers, and no codes or indirect identifiers that linked back to the subjects. The human PDAC tumor was cut into 3–5 mm^3 pieces with a razor blade on a sterilized petri dish. A small incision was made in the skin on the lower back of NSG mice, and the PDAC tumor was implanted subcutaneously. The tumor growth was monitored three times per week by digital caliper (Fisherbrand™ Traceable™ Digital Calipers).

Flow cytometry

Flow cytometric analysis of TDLNs was performed, and each leukocyte population was quantified. The TDLNs were placed onto a 70-μm cell strainer (BD Falcon), attached to a 50-ml conical tube. The TDLNs was mashed in sterile Dulbecco's Phosphate-Buffered Saline (DPBS) through the strainer using the plunger end of a syringe. The single-cell suspension was centrifuged at 340*g* for 5 min. The pellet was resuspended in complete RPMI 1640 at 1×10^7 cells/ml. Cells were plated in 96-well round-bottom plates (Corning, NY) for intracellular cytokine staining and 96-well flat-bottom plates (Corning, NY) for cell-surface and intracellular transcription factor staining. The cell samples that underwent intracellular cytokine staining were incubated first with 100 ng/ml PMA, 1 μg/ml ionomycin (Sigma-Aldrich), and GolgiStop™ protein transport inhibitor (BD Bioscience) at 37 °C for 4 h. All samples were washed with DPBS prior to incubation with Fixable Viability Dye eFluor™ 780 (Thermo Fisher Scientific) diluted 1:1000 in DPBS for 30 min at 4 °C. Then, the cells were washed with FACS buffer (DPBS + 2% fetal bovine serum +1 mM EDTA + 0.1% sodium azide) and incubated for 30 min at 4 °C with the following cell-surface antibodies: PB anti-CD4 (100428, Biolegend), BV510 anti-CD8 (100752, Biolegend), APC anti-CD44 (103012, Biolegend), PE/Cy7 anti-CD62L (104418, Biolegend), PE anti-CD25 (558642, BD Pharmingen), BV510 anti-CD45 (103138, Biolegend). All the cell-surface antibodies were diluted 1:300 in FACS buffer. The cells were permeabilized using the eBioscience Intracellular Fixation and Permeabilization Buffer Set (Thermo Fisher Scientific) for 30 min at 4 °C. Then, they were incubated with the following intracellular antibodies: PerCP/Cy5.5 anti-FoxP3 (45-5773-82, Invitrogen), APC anti-IFNγ (505810, Biolegend), FITC anti-TNFα (506304, Biolegend). All of the intracellular antibodies were diluted 1:300 in the eBioscience Permeabilization Buffer (1x) (Thermo Fisher Scientific). Cells were washed once with Permeabilization Buffer and fixed in FACS buffer containing 1% formalin. Flow cytometry was performed using a BD FACSCanto™ II flow cytometer (BD Biosciences). Analysis of flow cytometry results was performed via FlowJo software (FlowJo LLC, Ashland, OR).

RT-PCR assay

RNA was isolated with Quick-RNA MiniPrep kit (Zymo Research, Irvine, CA, USA), and the first strand of cDNA was synthesized using 2 μg of RNA and High-Capacity Reverse Transcriptase (Invitrogen). RT-PCR was performed with SYBR Green PCR reagents. RNA levels were normalized to the level of GAPDH and calculated as delta-delta threshold cycle (ΔΔCT). Primers used for RT-PCR are listed as follows: GAPDH-F:AGCCACATCGCTCAGACAC, GAPDH-R:GCCCAATACG ACCAAATCC; Fut7-F:AGCTGGAGGAGCAACATTCAT, Fut7-R:GGATGGT GAGTGTGGACTGAG; Chst2-F:CCGCTCGGGATGAAGGTATTT, Chst2-R: CCACTTGTAGTCCAAGAGGTTGA; Chst4-F:GGGTTCCCAGGTCATCG TTG, Chst4-R:CCGAAAAGCTGTCCCACAAAA; Glycam1-F:GTCCTGCTA TTTGTCAGTCTTGC, Glycam1-R: CCTGGGCCTCTTGATTCTCTG; Icam1-F:GTGATGCTCAGGTATCCATCCA, Icam1-R:CACAGTTCTCAAAGCACA GCG; Madcam1-F:CCTGGCCCTAGTACCCTACC, Madcam1-R:CCGTACA GAGAGGATACTGCTG; Cd34-F:GGTAGCTCTCTGCCTGATGAG, Cd34-R: TGGTAGGAACTGATGGGGATATT; Emcn-F:AATACCAGGCATCGTGTC AGT, Emcn-R:CTGATTCTCAGTCTTGTTCTGGG; Cd300lg-F:AAAGCCCC TGTATTCACCGAG, Cd300lg-R: CCTGCATGAGGAGAGGTCG; Podxl-F: GCCACCAAAGTGCCACAAC, Podxl-R:CGGCATAGATGGAGATTGGGTT. All RT-PCR reactions were performed in triplicate.

Antibody and Taxol conjugation

Glutaric anhydride (100 mg, Sigma-Aldrich) and Taxol (33 mg, LC laboratories) were prepared in a 4 ml vial, dried under high vacuum for 24 h and dissolved in 1 ml of pyridine. The solution was stirred at room temperature under Ar atmosphere for 2 h. The reaction was quenched by removal of solvent under high vacuum for 2 h. 2'-Glutaryl taxol was purified by a reversed phase HPLC (Phenomenex Luna 5 μm C18 250 × 10.0 mm, flow rate 2 ml/min, UV 250 nm detection) with a gradient solvent system (15–75% ACN/H2O with 0.1% formic acid for 40 min). 2'-glutaryl taxol (0.2 mg) dissolved in DMSO (Thermo Scientific Fisher) was activated with 1-ethyl-3-(3-dimethylaminopropyl)carbodiimide hydrochloride (EDC, 0.4 mg, Sigma-Aldrich) and Sulfo-NHS (N-hydroxysulfosuccinimide) (1.1 mg, Thermo Scientific Fisher) for 15 min at room temperature in MES buffer (pH 6.0, Thermo Scientific Fisher) (final solution; ~1 ml in 10% DMSO). The EDC was quenched by 2-mercaptoethanol (1.4 μL, Sigma-Aldrich) for 10 min. Immediately, the pH of solution was increased by $NaHCO_3$ (0.1 M, Sigma-Aldrich) to ~8. MHA112 dissolved in PBS (pH 7.4, Corning) was mixed with the activated 2'-glutaryl Taxol at room temperature for 2 h (1:20 molar ratio of MHA112 to Taxol, final solution; 10% DMSO). Dialysis was performed twice by a centrifugal filter (Amicon®, 10 kD MWCO, Sigma-Aldrich) at 10,000 rpm for 15 min to remove the free taxol. The solution was purified further by a desalting column (Zeba™, 7 kD MWCO, Thermo Scientific Fisher).

Determination of drug to antibody ratio (DAR) for MHA112-Taxol

Reverse-phase HPLC (RP-HPLC) was used to determine the DAR of antibody-drug conjugate. MHA112-taxol conjugates (1 mg/ml) were incubated with 40 mM DL-dithiothreitol (Sigma-Aldrich, USA) for 1 h at 37 °C to reduce the interchain disulfide bond. RP-HPLC was performed on both intact and reduced conjugates using the PLRP-S column (5 μm, 1000 Å, 2.1 × 50 mm from Agilent) coupled to Agilent 1260 Infinity II system. The samples were analyzed at 0.8 ml/min using 0.1% TFA in a water-acetonitrile gradient maintained at 70 °C. The reduced conjugate was resolved into a light and heavy chain fragments compared to the intact form. The peak area was quantified from the RP-HPLC chromatogram for the reduced MHA112-Taxol, which comprises of unconjugated light chain (L0) and heavy chain (H0) and conjugated light chain (L1) and heavy chains (H1). The experiment was done in triplicates and DAR was determined from the peak area of the reduced MHA112-Taxol conjugate using the standard equation.

$$DAR = 2\left(\frac{\text{Conjugated LC area}}{\text{Total LC peak area}} + \frac{\text{Conjugated HC area}}{\text{Total HC peak area}}\right)$$

Flow cytometry for antibody and antibody-drug conjugate internalization

CHO-PNAd cells (1×10^6 cells/ml) were incubated with 2 μg/ml MHA112 for 30 min on ice, rinsed with ice-cold PBS, and then incubated for 30 min. The cells were rinsed with cold PBS, resuspended in growth media, and incubated at 37 °C. The samples were harvested at various times and processed for flow cytometry. To detect internalized antibody, the cells were washed with cold PBS, incubated with proteinase K (1 μg/ml for 10 min at 37 °C), washed to remove cell surface-bound antibody, and incubated with the FITC anti-mouse IgM antibody (ab150121, Abcam). The cells were assessed by flow cytometry using a BD FACSCanto™ II flow cytometer (BD Biosciences). Analysis of flow cytometry results was performed via FlowJo software (FlowJo LLC, Ashland, OR). For inhibitors assay, CHO-PNAd cells were preincubated with inhibitors (20 μM methyl-β-cyclodextrin, 3 mM amiloride, 10 μg/ml chlorpromazine, 10 μg/ml nystatin; Sigma) for 30 min at 4 °C prior to a 3 h incubation with MHA112 at 37 °C. The cells were processed as described above for internalized antibody.

Statistical analysis

All experiments were repeated at least three times, each done in triplicate. The statistical significance between two groups was determined by unpaired Student's *t*-test, whereas comparisons between multiple groups were carried out by a repeated-measures two-way analysis of variance (ANOVA) with Tukey's test, an ordinary one-way ANOVA with Tukey's test or Dunnett's test, using GraphPad Prism 7 software (GraphPad Software, Inc., CA). A probability value of $^*P < 0.05$ was considered to be significant.

CRediT authorship contribution statement

L.J. designed and performed experiments, analyzed data, and wrote the main text of the manuscript. S.J. performed antibody conjugations experiments, analyzed data, and wrote parts of the Methods and Results. J.Z., T.I., and J.J. performed experiments, analyzed data. V.K., P.F., A.S.L., K.S., N.A., N.J., T.O.A., J.S.B., M.K., and K.U. helped with study design and critically revised the manuscript. R.A. designed the study, interpreted and analyzed data, and critically revised and finalized the manuscript.

Data availability

All data generated or analyzed for this study are available from the corresponding author upon reasonable request.

Declaration of Competing Interest

All authors declare that they have no competing interests. R.A holds equity in NanoTomer, Inc. a biotech company that has licensed certain patent applications from Mass General Brigham generated by R.A.

Acknowledgments

This work was supported in part by the National Institute of Allergy and Infectious Diseases and National Heart, Lung, and Blood Institute of the National Institutes of Health (NIH) under award numbers R01HL145813 (R.A.) and P01AI153003 (R.A., J.B.).

Appendix A. Supporting information

Supplementary data associated with this article can be found in the online version at doi:10.1016/j.nantod.2020.101045.

References

[1] E.G. Kim, K.M. Kim, Strategies and advancement in antibody-drug conjugate optimization for targeted cancer therapeutics, Biomol. Ther. 23 (2015) 493–509.
[2] D.M. Collins, B. Bossenmaier, G. Kollmorgen, G. Niederfellner, Cancers 11 (2019).
[3] A. Beck, L. Goetsch, C. Dumontet, N. Corvaia, Strategies and challenges for the next generation of antibody–drug conjugates, Nat. Rev. Drug Discov. 16 (2017) 315–337.
[4] M.R. Nejadmoghaddam, A. Minai-Tehrani, R. Ghahremanzadeh, M. Mahmoudi, R. Dinarvand, A.H. Zarnani, Avicenna J. Med. Biotechnol. 11 (2019) 3–23.
[5] Brentuximab vedotin with chemotherapy for stage III or IV Hodgkin's lymphoma, N. Engl. J. Med. 378 (2018) 878.
[6] D.R. Oostra, E.R. Macrae, Breast Cancer 6 (2014) 103–113.
[7] I.R. Yurkiewicz, L. Muffly, M. Liedtke, Inotuzumab ozogamicin: a CD22 mAb-drug conjugate for adult relapsed or refractory B-cell precursor acute lymphoblastic leukemia, Drug Des. Dev. Ther. 12 (2018) 2293–2300.
[8] M. Gbadamosi, S. Meshinchi, J.K. Lamba, Gemtuzumab ozogamicin for treatment of newly diagnosed CD33-positive acute myeloid leukemia, Futur. Oncol. 14 (2018) 3199–3213.
[9] B. Bahmani, I. Vohra, N. Kamaly, R. Abdi, Active targeted delivery of immune therapeutics to lymph nodes, Curr. Opin. Organ Transplant. 23 (2018) 8–14.
[10] S. Hemmerich, E.C. Butcher, S.D. Rosen, Sulfation-dependent recognition of high endothelial venules (HEV)-ligands by L-selectin and MECA 79, and adhesion-blocking monoclonal antibody, J. Exp. Med. 180 (1994) 2219–2226.
[11] S.Y. Lee, Q. Chao-Nan, O.A. Seng, C. Peiyi, W.H. Bernice, M.S. Swe, W.J. Chii, H.S. Jacqueline, S.K. Chee, Changes in specialized blood vessels in lymph nodes and their role in cancer metastasis, J. Transl. Med. 10 (2012) 206.
[12] N. Hiraoka, Y. Ino, R. Yamazaki-Itoh, Y. Kanai, T. Kosuge, K. Shimada, Intratumoral tertiary lymphoid organ is a favourable prognosticator in patients with pancreatic cancer, Br. J. Cancer 112 (2015) 1782–1790.
[13] N. Hiraoka, Y. Ino, R. Yamazaki-Itoh, Tertiary lymphoid organs in cancer tissues, Front. Immunol. 7 (2016) 244.
[14] E.J. Colbeck, A. Ager, A. Gallimore, G.W. Jones, Tertiary lymphoid structures in cancer: drivers of antitumor immunity, immunosuppression, or bystander sentinels in disease, Front. Immunol. 8 (2017) 1830.
[15] K. Alitalo, The lymphatic vasculature in disease, Nat. Med. 17 (2011) 1371–1380.
[16] R.C. Ji, Lymph nodes and cancer metastasis: new perspectives on the role of intranodal lymphatic sinuses, Int. J. Mol. Sci. 18 (2016) 51.
[17] Z. Gil, D.L. Carlson, J.O. Boyle, D.H. Kraus, J.P. Shah, A.R. Shaha, B. Singh, R.J. Wong, S.G. Patel, Lymph node density is a significant predictor of outcome in patients with oral cancer, Cancer 115 (2009) 5700–5710.
[18] L.P. Kowalski, R. Bagietto, J.R. Lara, R.L. Santos, J.F. Silva Jr., J. Magrin, Prognostic significance of the distribution of neck node metastasis from oral carcinoma, Head Neck 22 (2000) 207–214.
[19] D. Jones, E.R. Pereira, T.P. Padera, Growth and immune evasion of lymph node metastasis, Front. Oncol. 8 (2018) 36.
[20] S.N. Thomas, N.A. Rohner, E.E. Edwards, Implications of lymphatic transport to lymph nodes in immunity and immunotherapy, Annu. Rev. Biomed. Eng. 18 (2016) 207–233.
[21] G. Gerlini, C. Urso, G. Mariotti, P. Di Gennaro, D. Palli, P. Brandani, A. Salvadori, N. Pimpinelli, U.M. Reali, L. Borgognoni, Plasmacytoid dendritic cells represent a major dendritic cell subset in sentinel lymph nodes of melanoma patients and accumulate in metastatic nodes, Clin. Immunol. 125 (2007) 184–193.
[22] A. Battaglia, A. Buzzonetti, C. Baranello, G. Ferrandina, E. Martinelli, F. Fanfani, G. Scambia, A. Fattorossi, Metastatic tumour cells favour the generation of a tolerogenic milieu in tumour draining lymph node in patients with early cervical cancer, Cancer Immunol. Immunother. 58 (2009) 1363–1373.
[23] N.L. Trevaskis, L.M. Kaminskas, C.J. Porter, From sewer to saviour — targeting the lymphatic system to promote drug exposure and activity, Nat. Rev. Drug Discov. 14 (2015) 781–803.
[24] L. Milling, Y. Zhang, D.J. Irvine, Delivering safer immunotherapies for cancer, Adv. Drug Deliv. Rev. 114 (2017) 79–101.
[25] C.J. Batty, P. Tiet, E.M. Bachelder, K.M. Ainslie, Drug delivery for cancer immunotherapy and vaccines, Pharm. Nanotechnol. 6 (2019) 232–244.
[26] E.F.J. Meijer, C. Blatter, I.X. Chen, E. Bouta, D. Jones, E.R. Pereira, K. Jung, B.J. Vakoc, J.W. Baish, T.P. Padera, Lymph node effective vascular permeability and chemotherapy uptake, Microcirculation 24 (2017) e12381.
[27] J. Chen, L. Wang, Q. Yao, R. Ling, K. Li, H. Wang, Drug concentrations in axillary lymph nodes after lymphatic chemotherapy on patients with breast cancer, Breast Cancer Res. 6 (2004) R474–R477.
[28] A.O. Oladipo, O.S. Oluwafemi, S.P. Songca, A. Sukhbaatar, S. Mori, J. Okajima, A. Komiya, S. Maruyama, T. Kodama, A novel treatment for metastatic lymph nodes using lymphatic delivery and photothermal therapy, Sci. Rep. 7 (2017) 45459.
[29] K. Maisel, M.S. Sasso, L. Potin, M.A. Swartz, Exploiting lymphatic vessels for immunomodulation: rationale, opportunities, and challenges, Adv. Drug Deliv. Rev. 114 (2017) 43–59.

[30] D. Rosenblum, N. Joshi, W. Tao, J.M. Karp, D. Peer, Progress and challenges towards targeted delivery of cancer therapeutics, Nat. Commun. 9 (2018) 1410.
[31] T.N. Seyfried, L.C. Huysentruyt, On the origin of cancer metastasis, Crit. Rev. Oncog. 18 (2013) 43–73.
[32] A.W. Lambert, D.R. Pattabiraman, R.A. Weinberg, Emerging biological principles of metastasis, Cell 168 (2017) 670–691.
[33] C. Tang, X. Wang, H. Soh, S. Seyedin, M.A. Cortez, S. Krishnan, E. Massarelli, D. Hong, A. Naing, A. Diab, D. Gomez, H. Ye, J. Heymach, R. Komaki, J.P. Allison, P. Sharma, J.W. Welsh, Combining radiation and immunotherapy: a new systemic therapy for solid tumors, Cancer Immunol. Res. 2 (2014) 831–838.
[34] M.V. Zavyalova, E.V. Denisov, L.A. Tashireva, O.E. Savelieva, E.V. Kaigorodova, N.V. Krakhmal, V.M. Perelmuter, Intravasation as a key step in cancer metastasis, Biochemistry 84 (2019) 762–772.
[35] Y.D. Ko, Die Rolle der Systemtherapie bei Lungenmetastasen mit Lymphknotenbefall, Chirurg 90 (2019) 997–1002.
[36] Y. Fontebasso, S.M. Dubinett, Drug development for metastasis prevention, Crit. Rev. Oncog. 20 (2015) 449–473.
[37] W. Gu, C. Wu, J. Chen, Y. Xiao, Nanotechnology in the targeted drug delivery for bone diseases and bone regeneration, Int. J. Nanomed. 8 (2013) 2305–2317.
[38] C. D'Antonio, A. Passaro, B. Gori, E. Del Signore, M.R. Migliorino, S. Ricciardi, A. Fulvi, F. de Marinis, Bone and brain metastasis in lung cancer: recent advances in therapeutic strategies, Ther. Adv. Med. Oncol. 6 (2014) 101–114.
[39] K. Uchimura, J.M. Gauguet, M.S. Singer, D. Tsay, R. Kannagi, T. Muramatsu, U.H. von Andrian, S.D. Rosen, A major class of L-selectin ligands is eliminated in mice deficient in two sulfotransferases expressed in high endothelial venules, Nat. Immunol. 6 (2005) 1105–1113.
[40] M. Kobayashi, J. Mitoma, H. Hoshino, S.Y. Yu, Y. Shimojo, K. Suzawa, K.H. Khoo, M. Fukuda, J. Nakayama, Prominent expression of sialyl Lewis X-capped core 2-branchedO-glycans on high endothelial venule-like vessels in gastric MALT lymphoma: high endothelial venule-like vessels in gastric MALT lymphoma, J. Pathol. 224 (2011) 67–77.
[41] A. Dal Corso, S. Cazzamalli, R. Gebleux, M. Mattarella, D. Neri, Protease-cleavable linkers modulate the anticancer activity of noninternalizing antibody–drug conjugates, Bioconjugate Chem. 28 (2017) 1826–1833.
[42] M.S. Sutherland, R.J. Sanderson, K.A. Gordon, J. Andreyka, C.G. Cerveny, C. Yu, T.S. Lewis, D.L. Meyer, R.F. Zabinski, S.O. Doronina, P.D. Senter, C.L. Law, A.F. Wahl, Lysosomal trafficking and cysteine protease metabolism confer target-specific cytotoxicity by peptide-linked Anti-CD30-Auristatin conjugates, J. Biol. Chem. 281 (2006) 10540–10547.
[43] G. Sahay, D.Y. Alakhova, A.V. Kabanov, Endocytosis of nanomedicines, J. Control. Release 145 (2010) 182–195.
[44] S. Mayor, R.E. Pagano, Pathways of clathrin-independent endocytosis, Nat. Rev. Mol. Cell Biol. 8 (2007) 603–612.
[45] M.I. Harrell, B.M. Iritani, A. Ruddell, Tumor-induced sentinel lymph node lymphangiogenesis and increased lymph flow precede melanoma metastasis, Am. J. Pathol. 170 (2007) 774–786.
[46] H. Gonzalez, C. Hagerling, Z. Werb, Roles of the immune system in cancer: from tumor initiation to metastatic progression, Genes Dev. 32 (2018) 1267–1284.
[47] J.L. Messerschmidt, G.C. Prendergast, G.L. Messerschmidt, How cancers escape immune destruction and mechanisms of action for the new significantly active immune therapies: helping nonimmunologists decipher recent advances, Oncologist 21 (2016) 233–243.
[48] M. Zippi, G. De Toma, G. Minervini, C. Cassieri, R. Pica, D. Colarusso, S. Stock, P. Crispino, Desmoplasia influenced recurrence of disease and mortality in stage III colorectal cancer within five years after surgery and adjuvant therapy, Saudi J. Gastroenterol. 23 (2017) 39–44.
[49] B. Rybinski, J. Franco-Barraza, E. Cukierman, The wound healing, chronic fibrosis, and cancer progression triad, Physiol. Genom. 46 (2014) 223–244.
[50] P. Rawla, T. Sunkara, V. Gaduputi, Epidemiology of pancreatic cancer: global trends, etiology and risk factors, World J. Oncol. 10 (2019) 10–27.
[51] B. Bahmani, M. Uehara, F. Ordikhani, X. Li, L. Jiang, N. Banouni, T. Ichimura, V. Kasinath, S.K. Eskandari, N. Annabi, J.S. Bromberg, L.D. Shultz, D.L. Greiner, R. Abdi, Ectopic high endothelial venules in pancreatic ductal adenocarcinoma: a unique site for targeted delivery, EBioMedicine 38 (2018) 79–88.
[52] M. Ritchie, L. Tchistiakova, N. Scott, Implications of receptor-mediated endocytosis and intracellular trafficking dynamics in the development of antibody drug conjugates, MAbs 5 (2013) 13–21.
[53] K.E. Knewtson, C. Perera, D. Hymel, Z. Gao, M.M. Lee, B.R. Peterson, Antibody–drug conjugate that exhibits synergistic cytotoxicity with an endosome–disruptive peptide, ACS Omega 4 (2019) 12955–12968.
[54] Y.V. Kovtun, C.A. Audette, Y. Ye, H. Xie, M.F. Ruberti, S.J. Phinney, B.A. Leece, T. Chittenden, W.A. Blattler, V.S. Goldmacher, Antibody-drug conjugates designed to eradicate tumors with homogeneous and heterogeneous expression of the target antigen, Cancer Res. 66 (2006) 3214–3221.
[55] Y.V. Kovtun, V.S. Goldmacher, Cell killing by antibody–drug conjugates, Cancer Lett. 255 (2007) 232–240.
[56] B. Sammet, C. Steinkuhler, N. Sewald, Antibody–drug conjugates in tumor therapy, Pharm. Pat. Anal. 1 (2012) 65–73.
[57] L.Y. Wang, I. Ganly, Nodal metastases in thyroid cancer: prognostic implications and management, Future Oncol. 12 (2016) 981–994.
[58] M.A. Swartz, A.W. Lund, Lymphatic and interstitial flow in the tumour microenvironment: linking mechanobiology with immunity, Nat. Rev. Cancer 12 (2012) 210–219.
[59] M.F. Fransen, R. Arens, C.J. Melief, Local targets for immune therapy to cancer: tumor draining lymph nodes and tumor microenvironment, Int. J. Cancer 132 (2013) 1971–1976.
[60] T. Liu, C. Han, S. Wang, P. Fang, Z. Ma, L. Xu, R. Yin, Cancer-associated fibroblasts: an emerging target of anti-cancer immunotherapy, J. Hematol. Oncol. 12 (2019) 86.
[61] T. Liu, L. Zhou, D. Li, T. Andl, Y. Zhang, Cancer-associated fibroblasts build and secure the tumor microenvironment, Front. Cell Dev. Biol. 7 (2019) 60.
[62] E.M. Pritchard, M.A. Dyer, R.K. Guy, Progress in small molecule therapeutics for the treatment of retinoblastoma, Mini-Rev. Med. Chem. 16 (2016) 430–454.
[63] S. Han, K. Huang, Z. Gu, J. Wu, Tumor immune microenvironment modulation-based drug delivery strategies for cancer immunotherapy, Nanoscale 12 (2020) 413–436.
[64] I.F. Tannock, C.M. Lee, J.K. Tunggal, D.S. Cowan, M.J. Egorin, Clin. Cancer Res. 8 (2002) 878–884.
[65] P.M. Chang, C.T. Cheng, R.C. Wu, Y.H. Chung, K.C. Chiang, T.S. Yeh, C.Y. Liu, M.H. Chen, C.N. Yeh, Oncol. Lett. 16 (2018) 566–572.
[66] T. Miyashita, H. Tajima, I. Makino, M. Okazaki, T. Yamaguchi, Y. Ohbatake, S. Nakanuma, H. Hayashi, H. Takamura, I. Ninomiya, S. Fushida, K. Kishimoto, J.W. Harmon, T. Ohta, Anticancer Res. 38 (2018) 337–343.
[67] R. Feng, Y. Morine, T. Ikemoto, S. Imura, S. Iwahashi, Y. Saito, M. Shimada, Nab-paclitaxel interrupts cancer-stromal interaction through C-X-C motif chemokine 10-mediated interleukin-6 downregulation in vitro, Cancer Sci. 109 (2018) 2509–2519.
[68] M.J. Ernsting, B. Hoang, I. Lohse, E. Undzys, P. Cao, T. Do, B. Gill, M. Pintilie, D. Hedley, S.D. Li, Targeting of metastasis-promoting tumor-associated fibroblasts and modulation of pancreatic tumor-associated stroma with a carboxymethylcellulose-docetaxel nanoparticle, J. Control. Release 206 (2015) 122–130.
[69] O.H. Maarouf, M. Uehara, V. Kasinath, Z. Solhjou, N. Banouni, B. Bahmani, L. Jiang, O.A. Yilmam, I. Guleria, S.B. Lovitch, J.L. Grogan, P. Fiorina, P.T. Sage, J.S. Bromberg, M.M. McGrath, R. Abdi, Repetitive ischemic injuries to the kidneys result in lymph node fibrosis and impaired healing, JCI Insight 3 (2018).
[70] V. Saxena, L. Li, C. Paluskievicz, V. Kasinath, A. Bean, R. Abdi, C.M. Jewell, J.S. Bromberg, Role of lymph node stroma and microenvironment in T cell tolerance, Immunol. Rev. 292 (2019) 9–23.
[71] X. Li, A. Bean, M. Uehara, N. Banouni, M. Ben Nasr, V. Kasinath, L. Jiang, P. Fiorina, R. Abdi, Immune heterogeneity of head and tail pancreatic lymph nodes in non-obese diabetic mice, Sci. Rep. 9 (2019) 9778.
[72] L. Lin, X. Hu, H. Zhang, H. Hu, Tertiary lymphoid organs in cancer immunology: mechanisms and the new strategy for immunotherapy, Front. Immunol. 10 (2019) 1398.
[73] C.M. Paluskievicz, X. Cao, R. Abdi, P. Zheng, Y. Liu, J.S. Bromberg, T regulatory cells and priming the suppressive tumor microenvironment, Front. Immunol. 10 (2019) 2453.
[74] M.G. Lechner, S.M. Russell, R.S. Bass, A.L. Epstein, Chemokines, costimulatory molecules and fusion proteins for the immunotherapy of solid tumors, Immunotherapy 3 (2011) 1317–1340.
[75] G. Chatterjee, T. Pai, T. Hardiman, K. Avery-Kiejda, R.J. Scott, J. Spencer, S.E. Pinder, A. Grigoriadis, Molecular patterns of cancer colonisation in lymph nodes of breast cancer patients, Breast Cancer Res. 20 (2018) 143.
[76] J.H. Joo, Y.S. Kim, J.H. Nam, Prognostic significance of lymph node ratio in node-positive cervical cancer patients, Medicine 97 (2018) e11711.
[77] B. Chaudhary, E. Elkord, Vaccines 4 (2016).
[78] Y.A. Wang, X.L. Li, Y.Z. Mo, C.M. Fan, L. Tang, F. Xiong, C. Guo, B. Xiang, M. Zhou, J. Ma, X. Huang, X. Wu, Y. Li, G.Y. Li, Z.Y. Zeng, W. Xiong, Effects of tumor metabolic microenvironment on regulatory T cells, Mol. Cancer 17 (2018) 168.
[79] A. Verma, R. Mathur, A. Farooque, V. Kaul, S. Gupta, B.S. Dwarakanath, T-regulatory cells in tumor progression and therapy, Cancer Manag. Res. 11 (2019) 10731–10747.
[80] Y. Togashi, K. Shitara, H. Nishikawa, Regulatory T cells in cancer immunosuppression — implications for anticancer therapy, Nat. Rev. Clin. Oncol. 16 (2019) 356–371.
[81] B. Shang, Y. Liu, S.J. Jiang, Y. Liu, Prognostic value of tumor-infiltrating FoxP3+ regulatory T cells in cancers: a systematic review and meta-analysis, Sci. Rep. 5 (2015) 15179.
[82] X. Zhang, S. Kelaria, J. Kerstetter, J. Wang, J. Gastrointest. Oncol. 6 (2015) 307–313.
[83] A. Tanaka, S. Sakaguchi, Regulatory T cells in cancer immunotherapy, Cell Res. 27 (2017) 109–118.
[84] A.R. Sanchez-Paulete, A. Teijeira, J.I. Quetglas, M.E. Rodriguez-Ruiz, A. Sanchez-Arraez, S. Labiano, I. Etxeberria, A. Azpilikueta, E. Bolanos, M.C. Ballesteros-Briones, N. Casares, S.A. Quezada, P. Berraondo, D. Sancho, C. Smerdou, I. Melero, Intratumoral immunotherapy with XCL1 and sFlt3L encoded in recombinant Semliki Forest Virus–derived vectors fosters dendritic cell–mediated T-cell cross-priming, Cancer Res. 78 (2018) 6643–6654.
[85] M.L. Broz, M. Binnewies, B. Boldajipour, A.E. Nelson, J.L. Pollack, D.J. Erle, A. Barczak, M.D. Rosenblum, A. Daud, D.L. Barber, S. Amigorena, L.J. Van't Veer, A.I. Sperling, D.M. Wolf, M.F. Krummel, Dissecting the tumor myeloid compartment reveals rare activating antigen-presenting cells critical for T cell immunity, Cancer Cell 26 (2014) 938.
[86] C.S. Garris, S.P. Arlauckas, R.H. Kohler, M.P. Trefny, S. Garren, C. Piot, C. Engblom, C. Pfirschke, M. Siwicki, J. Gungabeesoon, G.J. Freeman, S.E. Warren, S. Ong, E. Browning, C.G. Twitty, R.H. Pierce, M.H. Le, A.P. Algazi, A.I. Daud, S.I. Pai, A. Zippelius, R. Weissleder, M.J. Pittet, Successful Anti-PD-1 cancer immunotherapy requires T cell-dendritic cell crosstalk involving the cytokines IFN-γ and IL-12, Immunity 49 (2018) 1148–1161.e7.
[87] L.W. Pfannenstiel, S.S. Lam, L.A. Emens, E.M. Jaffee, T.D. Armstrong, Paclitaxel enhances early dendritic cell maturation and function through TLR4 signaling in mice, Cell. Immunol. 263 (2010) 79–87.

[88] T. Michels, G.V. Shurin, H. Naiditch, A. Sevko, V. Umansky, M.R. Shurin, Paclitaxel promotes differentiation of myeloid-derived suppressor cells into dendritic cellsin vitroin a TLR4-independent manner, J. Immunotoxicol. 9 (2012) 292–300.
[89] J. John, M. Ismail, C. Riley, J. Askham, R. Morgan, A. Melcher, H. Pandha, Differential effects of Paclitaxel on dendritic cell function, BMC Immunol. 11 (2010) 14.
[90] B. Maier, A.M. Leader, S.T. Chen, N. Tung, C. Chang, J. LeBerichel, A. Chudnovskiy, S. Maskey, L. Walker, J.P. Finnigan, M.E. Kirkling, B. Reizis, S. Ghosh, N.R. D'Amore, N. Bhardwaj, C.V. Rothlin, A. Wolf, R. Flores, T. Marron, A.H. Rahman, E. Kenigsberg, B.D. Brown, M. Merad, A conserved dendritic-cell regulatory program limits antitumour immunity, Nature 580 (2020) 257–262.
[91] Y. Xie, T.R. Bagby, M.S. Cohen, M.L. Forrest, Drug delivery to the lymphatic system: importance in future cancer diagnosis and therapies, Expert Opin. Drug Deliv. 6 (2009) 785–792.
[92] C. Oussoren, G. Storm, Liposomes to target the lymphatics by subcutaneous administration, Adv. Drug Deliv. Rev. 50 (2001) 143–156.
[93] P. Maincent, P. Thouvenot, C. Amicabile, M. Hoffman, J. Kreuter, P. Couvreur, J.P. Devissaguet, Pharm. Res. 09 (1992) 1534–1539.
[94] H. Fujii, S. Horie, K. Takeda, S. Mori, T. Kodama, Optimal range of injection rates for a lymphatic drug delivery system, J. Biophotonics 11 (2018) e201700401.
[95] S. Kato, Y. Shirai, M. Sakamoto, S. Mori, T. Kodama, Use of a lymphatic drug delivery system and sonoporation to target malignant metastatic breast cancer cells proliferating in the marginal sinuses, Sci. Rep. 9 (2019) 13242.
[96] B. Bahmani, M. Uehara, L. Jiang, F. Ordikhani, N. Banouni, T. Ichimura, Z. Solhjou, G.J. Furtmuller, G. Brandacher, D. Alvarez, U.H. von Andrian, K. Uchimura, Q. Xu, I. Vohra, O.A. Yilmam, Y. Haik, J. Azzi, V. Kasinath, J.S. Bromberg, M.M. McGrath, R. Abdi, Targeted delivery of immune therapeutics to lymph nodes prolongs cardiac allograft survival, J. Clin. Investig. 128 (2018) 4770–4786.
[97] E. Allen, A. Jabouille, L.B. Rivera, I. Lodewijckx, R. Missiaen, V. Steri, K. Feyen, J. Tawney, D. Hanahan, I.P. Michael, G. Bergers, Combined antiangiogenic and anti–PD-L1 therapy stimulates tumor immunity through HEV formation, Sci. Transl. Med. 9 (2017) eaak9679.
[98] M. Fankhauser, M.A.S. Broggi, L. Potin, N. Bordry, L. Jeanbart, A.W. Lund, E. Da Costa, S. Hauert, M. Rincon-Restrepo, C. Tremblay, E. Cabello, K. Homicsko, O. Michielin, D. Hanahan, D.E. Speiser, M.A. Swartz, Tumor lymphangiogenesis promotes T cell infiltration and potentiates immunotherapy in melanoma, Sci. Transl. Med. 9 (2017) eaal4712.
[99] S. Bayraktar, C.M. Rocha-Lima, Advanced or metastatic pancreatic cancer: molecular targeted therapies, Mt. Sinai J. Med. 77 (2010) 606–619.
[100] H. Dillekas, M.S. Rogers, O. Straume, Are 90% of deaths from cancer caused by metastases, Cancer Med. 8 (2019) 5574–5576.
[101] L. Zhang, H. Su, Y. Liu, N. Pang, J. Li, X.R. Qi, Enhancing solid tumor therapy with sequential delivery of dexamethasone and docetaxel engineered in a single carrier to overcome stromal resistance to drug delivery, J. Control. Release 294 (2019) 1–16.
[102] Y. Xia, B. Zhang, H. Zhang, W. Li, K.P. Wang, H. Shen, J. Thorac. Dis. 7 (2015) S231–S237.
[103] X. Zhou, X. Ou, Y. Yang, T. Xu, C. Shen, J. Ding, C. Hu, Quantitative metastatic lymph node regions on magnetic resonance imaging are superior to AJCC N classification for the prognosis of nasopharyngeal carcinoma, J. Oncol. 2018 (2018) 1–10.
[104] R.G. Majzner, C.L. Mackall, Tumor antigen escape from CAR T-cell therapy, Cancer Discov. 8 (2018) 1219–1226.
[105] R.D. Salinas, J.S. Durgin, D.M. O'Rourke, Potential of glioblastoma-targeted chimeric antigen receptor (CAR) T-Cell therapy, CNS Drugs 34 (2020) 127–145.
[106] S.S. Bacus, A.V. Gudkov, M. Lowe, L. Lyass, Y. Yung, A.P. Komarov, K. Keyomarsi, Y. Yarden, R. Seger, Taxol-induced apoptosis depends on MAP kinase pathways (ERK and p38) and is independent of p53, Oncogene 20 (2001) 147–155.
[107] Narentuya, Y. Takeda-Uchimura, T. Foyez, Z. Zhang, T.O. Akama, H. Yagi, K. Kato, Y. Komatsu, K. Kadomatsu, K. Uchimura, GlcNAc6ST3 is a keratan sulfate sulfotransferase for the protein-tyrosine phosphatase PTPRZ in the adult brain, Sci. Rep. 9 (2019) 4387.

Figure S1.

(A) Fluorescence micrographs of CHO-PNAd cells confirmed MHA112 binding. MECA-79 was used for positive control. Scale bar: 100μm. (B) Isotyping ELISA showed that MHA112 was a mouse IgM antibody. (C) Fluorescence micrographs and semiquantitative analysis showed that the fluorescence intensities of MHA112-IR800 and free IR800 were not significantly different. NS (no significant difference). (D) Fluorescence micrographs and semiquantitative analysis of mouse LNs showed colocalization of MHA112-IR800 with CD11c, PDPN, CD11b, and ER-TR7. Scale bar: 20μm. **p < 0.01.

Figure S2.

(A) Reverse-phase HPLC (RP-HPLC) was used to determine the DAR of antibody-drug conjugate. Reverse-phase-HPLC chromatograms of intact and reduced MHA112-taxol conjugate were analyzed at 214 nm. The peak area was quantified from the RP-HPLC chromatogram for the reduced MHA112-taxol conjugate, which is comprised of unconjugated light chain (L0) and heavy chain (H0), as well as conjugated light chain (L1) and heavy chain (H1). The DAR was determined as 2.811 ± 0.12 from the peak area of the reduced MHA112-Taxol conjugate, using the standard equation. (B) Fluorescence micrographs and semiquantitative analysis indicated that the HEV density in tumors was not significantly different in the control, free Taxol, and MHA112-Taxol groups. NS (no significant difference). Scale bar: 100μm. (C-D) *In vitro* fluorescence imaging of whole organs showed bio-distribution of free IR800, isotype control-IR800, and MHA112-IR800 to TDLNs, tumor, and organs at 24 hr. post injection. Semiquantitative analysis provided in D. Data are expressed as means ± SEM. **P < 0.01, ***P < 0.001, NS (no significant difference). (E) The graph shows comparison between the half-life ($t_{1/2}$) of free Taxol* ($t_{1/2}$=1.98hr.), isotype control-Taxol* ($t_{1/2}$=26.72hr.), and MHA112-Taxol* ($t_{1/2}$=24.80hr.) in the circulation.

Figure S3.

Flow cytometry analysis revealed higher percentages of $CD8^+TNF\alpha^+$ and $CD8^+IFN\gamma^+$ T cells, and lower percentage of $CD4^+CD25^+FoxP3^+$ Tregs in the 4T1mouse breast tumors of the MHA112-Taxol-treated group than the free Taxol-treated and control groups at 25 days post-implantation. All listed populations were gated under the $CD3^+CD45^+$ cell population. Data are expressed as means ± SEM. *P < 0.05.

Fig. S1

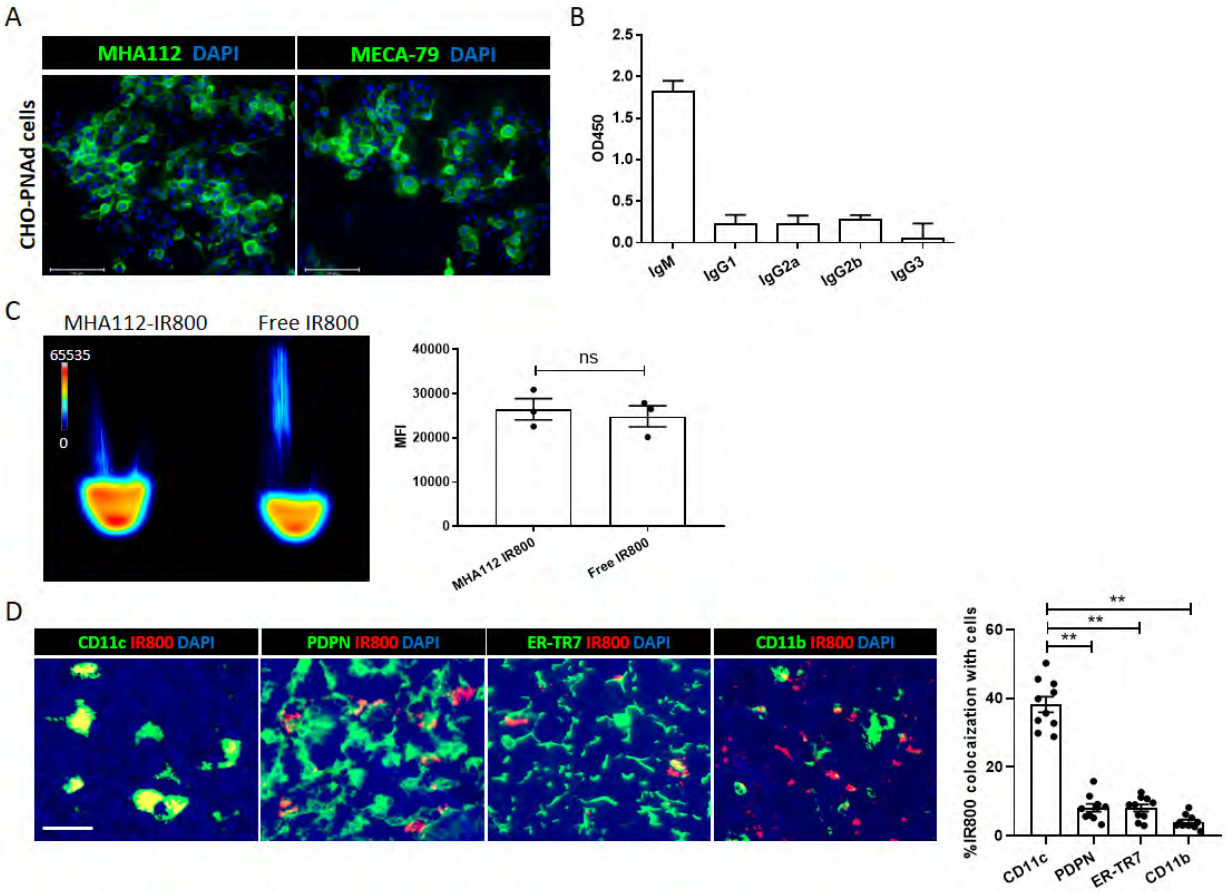
A
MHA112 DAPI
MECA-79 DAPI
CHO-PNAd cells
B
OD450
2.5
2.0
1.5
1.0
0.5
0.0
IgM
IgG1
IgG2a
IgG2b
IgG3
C
MHA112-IR800
Free IR800
65535
0
MFI
40000
30000
20000
10000
0
ns
MHA112 IR800
Free IR800
D
CD11c IR800 DAPI
PDPN IR800 DAPI
ER-TR7 IR800 DAPI
CD11b IR800 DAPI
%IR800 colocaization with cells
60
40
20
0
**
**
**
CD11c
PDPN
ER-TR7
CD11b

Fig. S2

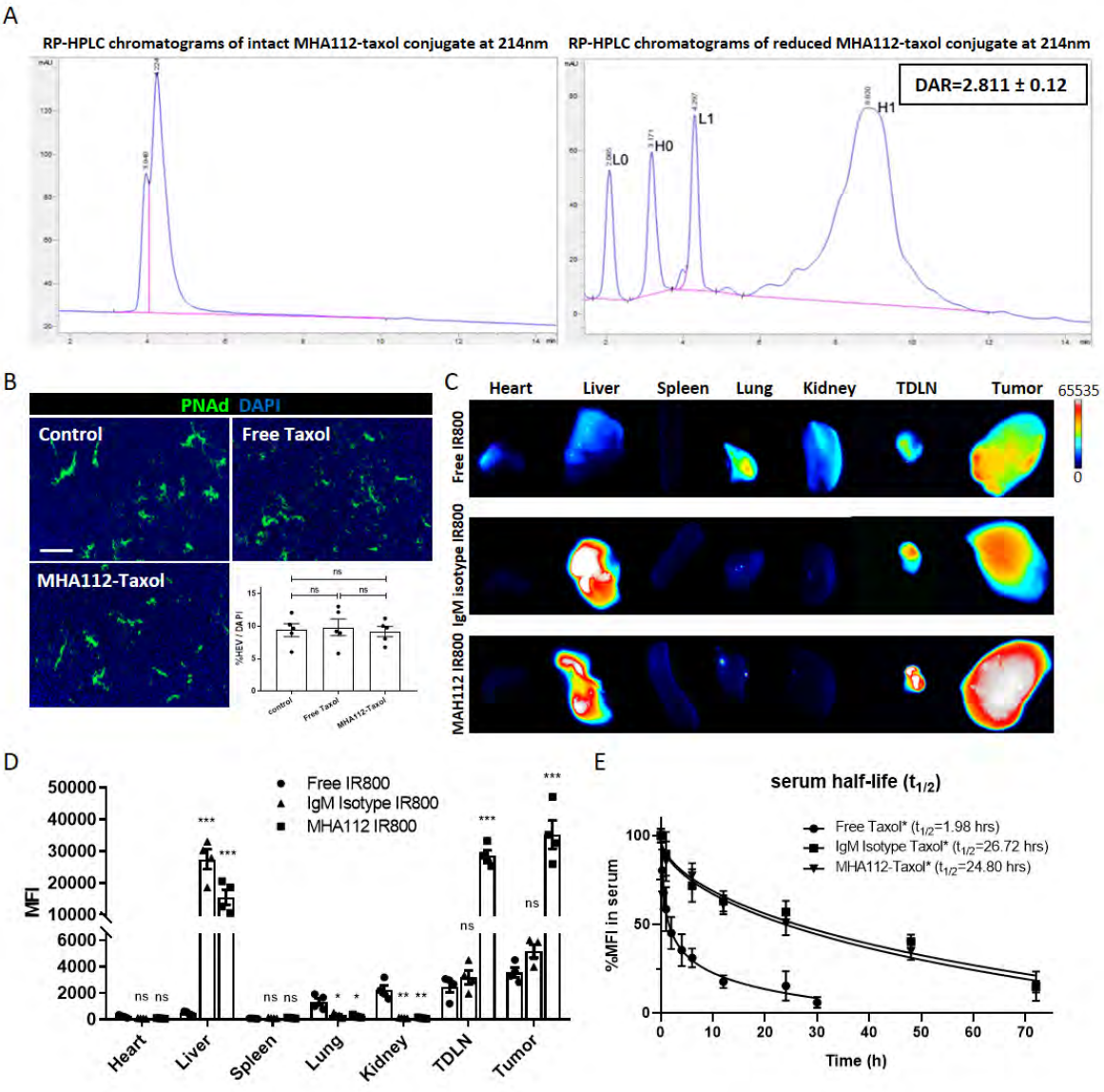
A
RP-HPLC chromatograms of intact MHA112-taxol conjugate at 214nm
RP-HPLC chromatograms of reduced MHA112-taxol conjugate at 214nm
DAR=2.811 ± 0.12
L0
H0
L1
H1
B
PNAd DAPI
Control
Free Taxol
MHA112-Taxol
%HEV / DAPI
C
Heart
Liver
Spleen
Lung
Kidney
TDLN
Tumor
65535
0
Free IR800
IgM isotype IR800
MAH112 IR800
D
Free IR800
IgM Isotype IR800
MHA112 IR800
MFI
E
serum half-life ($t_{1/2}$)
Free Taxol* ($t_{1/2}$=1.98 hrs)
IgM Isotype Taxol* ($t_{1/2}$=26.72 hrs)
MHA112-Taxol* ($t_{1/2}$=24.80 hrs)
%MFI in serum
Time (h)

Fig. S3

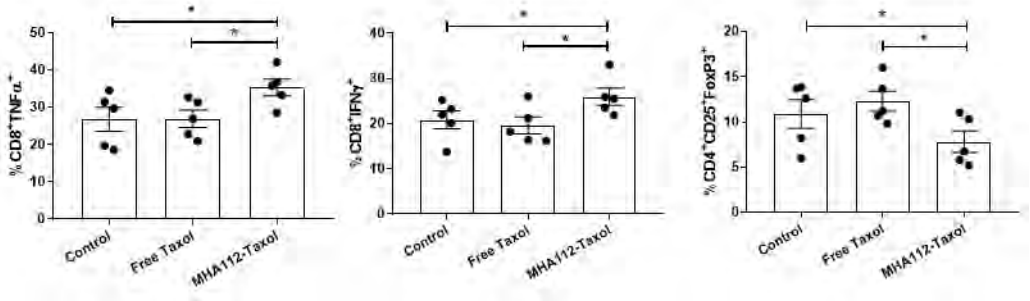
% CD8+TNFα+
% CD8+IFNγ+
% CD4+CD25+FoxP3+
Control
Free Taxol
MHA112-Taxol